

Empirical and Numerical Modeling of T-Phase Propagation from Ocean to Land

Approved for public release; distribution is unlimited.

July 2003



Prepared for:
Defense Threat Reduction Agency
8725 John J. Kingman Road, MS- 6201
Fort Belvoir, VA 22060-6201

20031017 099

DSWA01-97-C-0166

Jeffrey Stevens, et. al.

Prepared by:

Science Applications International Corporation
10260 Campus Point Drive
San Diego, CA 92121-1578

Technical Report

DESTRUCTION NOTICE

Destroy this report when it is no longer needed.
Do not return to sender.

PLEASE NOTIFY THE DEFENSE THREAT REDUCTION
AGENCY, ATTN: IMMI, 8725 JOHN J. KINGMAN ROAD,
MS-6201, FT BELVOIR, VA 22060-6201, IF YOUR ADDRESS
IS INCORRECT, IF YOU WISH IT DELETED FROM THE
DISTRIBUTION LIST, OR IF THE ADDRESSEE IS NO
LONGER EMPLOYED BY YOUR ORGANIZATION.

DISTRIBUTION LIST UPDATE

This mailer is provided to enable DTRA to maintain current distribution lists for reports. (We would appreciate you providing the requested information.)

- ☐ Add the individual listed to your distribution list.
- ☐ Delete the cited organization/individual.
- ☐ Change of address.

Note:

Please return the mailing label from the document so that any additions, changes, corrections or deletions can be made easily. For distribution cancellation or more information call DTRA/IMMI (703 767-4726).

NAME: _____

ORGANIZATION: _____

OLD ADDRESS

NEW ADDRESS

TELEPHONE NUMBER: () _____

DTRA PUBLICATION NUMBER/TITLE

CHANGES/DELETIONS/ADDITONS, etc.
(Attach Sheet if more Space is Required)

DTRA or other GOVERNMENT CONTRACT NUMBER: _____

CERTIFICATION of NEED-TO-KNOW BY GOVERNMENT SPONSOR (if other than DTRA):

SPONSORING ORGANIZATION: _____

CONTRACTING OFFICER or REPRESENTATIVE: _____

SIGNATURE: _____

DEFENSE THREAT REDUCTION AGENCY
ATTN: IMMI
8725 John J. Kingman Road, MS-6201
Ft Belvoir, VA 22060-6201

DEFENSE THREAT REDUCTION AGENCY
ATTN: IMMI
8725 John J. Kingman Road, MS-6201
Ft Belvoir, VA 22060-6201

| REPORT DOCUMENTATION PAGE | | | Form Approved OMB No. 0704-0188 | |
|--|--|---|------------------------------------|---------------------------|
| <small>Public reporting burden for this collection of information is estimated to average 1 hour per response, including the time for reviewing instructions, searching existing data sources, gathering and maintaining the data needed, and completing and reviewing the collection of information. Send comments regarding this burden estimate or any other aspect of this collection of information, including suggestions for reducing this burden, to Washington Headquarters Services, Directorate for Information Operations and Reports, 1215 Jefferson Davis Highway, Suite 1204, Arlington VA 22202-4302, and to the Office of Management and Budget, Paperwork Reduction Project (0704-0188), Washington, DC 20503.</small> | | | | |
| 1. AGENCY USE ONLY (Leave blank) | 2. REPORT DATE July 2003 | 3. REPORT TYPE AND DATES COVERED Technical 970926 - 001231 | | |
| 4. TITLE AND SUBTITLE Empirical and Numerical Modeling of T-Phase Propagation from Ocean to Land | | 5. FUNDING NUMBERS C - DSWA01-97-C-0166 PE - RDT & E PR - CD TA - CD WU - DH 65161 | | |
| 6. AUTHOR(S) Jeffrey Stevens, G.Eli Baker, Heming Xu, and Ron Cook (SAIC) Gerald D'Spain, Lewis P. Berger, and Lucie Pautet (Scripps) | | | | |
| 7. PERFORMING ORGANIZATION NAME(S) AND ADDRESS(ES) Science Applications International Corporation 10260 Campus Point Drive San Diego, CA 92121-1578 | | 8. PERFORMING ORGANIZATION REPORT NUMBER MTSD-DTR-00-16622 | | |
| 9. SPONSORING/MONITORING AGENCY NAME(S) AND ADDRESS(ES) Defense Threat Reduction Agency 8725 John J. Kingman Road, MS 6201 Fort Belvoir, VA 22060-6201 TDND/Dainty | | 10. SPONSORING/MONITORING AGENCY REPORT NUMBER DTRA-TR-01-15 | | |
| 11. SUPPLEMENTARY NOTES This work was sponsored by the Defense Threat Reduction Agency under RDT&E RMC code B 4698 C CD CD 65161 5P50 A 25904D. | | | | |
| 12a. DISTRIBUTION/AVAILABILITY STATEMENT Approved for public release; distribution is unlimited. | | 12b. DISTRIBUTION CODE | | |
| 13. ABSTRACT (Maximum 200 words) We use empirical and numerical methods to model propagation of T-phases from ocean to land. The empirical study uses data from pressure sensors in the ocean and coastal and island seismometers to measure the T-phase transfer function. The numerical study uses finite difference calculations to model T-phase propagation and conversion. We perform a detailed empirical and numerical study of the transition from the Point Sur IMS station to seismic stations along the California coast, and perform numerical calculations for IMS stations VIB, Tristan da Cunha and Ascension Island. We find both empirically and numerically the unusual result that converted surface waves arrive at coastal stations earlier than body waves. T-phases propagate primarily as P-waves once they are well inland from the coast. Calculations for slopes varying from 10 to 30 degrees are very similar. All IMS T-Phase stations are located in areas where the offshore slope is less than 30 degrees. We perform an analysis of observed waveforms under water and on land recorded during the Ascension Island experiment and find good agreement with the calculations. T-phase conversion attenuates higher frequencies, however high frequency energy from underwater explosion sources can still be observed at T-phase stations. | | | | |
| 14. SUBJECT TERMS Hydroacoustic T-phase | | Finite Difference IMS | | 15. NUMBER OF PAGES 60 |
| | | | | 16. PRICE CODE |
| 17. SECURITY CLASSIFICATION OF REPORT UNCLASSIFIED | 18. SECURITY CLASSIFICATION OF THIS PAGE UNCLASSIFIED | 19. SECURITY CLASSIFICATION OF ABSTRACT UNCLASSIFIED | 20. LIMITATION OF ABSTRACT SAR | |

UNCLASSIFIED

SECURITY CLASSIFICATION OF THIS PAGE

CLASSIFIED BY:

N/A since Unclassified

DECLASSIFIED BY:

N/A since Unclassified

7. PERFORMING ORGANIZATION NAME(S) AND ADDRESS(ES) (continued)

University of California - San Diego
Scripps Institution of Oceanography
Marine Physical Laboratory
P.O. Box 6049
San Diego, CA 92166-6049

SECURITY CLASSIFICATION OF THIS PAGE

UNCLASSIFIED

Conversion Table

| <i>Conversion factors for U.S. Customary to metric (SI) units of measurement</i> | | |
|--|-----------------------------------|--|
| MULTIPLY TO GET | BY | TO GET DIVIDE |
| angstrom | 1.000 000 X E -10 | meters (m) |
| atmosphere (normal) | 1.013 25 X E +2 | kilo pascal (kPa) |
| bar | 1.000 000 X E +2 | kilo pascal (kPa) |
| barn | 1.000 000 X E -28 | meter ² (m ²) |
| British thermal unit (thermochemical) | 1.054 350 X E +3 | joule (J) |
| calorie (thermochemical) | 4.184 000 | joule (J) |
| cal (thermochemical)/cm ² | 4.184 000 X E -2 | mega joule/m ² (MJ/m ²) |
| curie | 3.700 000 C E +1 | * giga becquerel (GBq) |
| degree (angle) | 1.745 329 X E -2 | radian (rad) |
| degree Fahrenheit | $t_k = (t^{\circ}f + 459.67)/1.8$ | degree kelvin (K) |
| electron volt | 1.602 19 X E -19 | joule (J) |
| erg | 1.000 000 X E -7 | joule (J) |
| erg/second | 1.000 000 X E -7 | watt (W) |
| foot | 3.048 000 X E -1 | meter (m) |
| foot-pound-force | 1.355 818 | joule (J) |
| gallon (U.S. liquid) | 3.785 412 X E -3 | meter ³ (m ³) |
| inch | 2.540 000 X E -2 | meter (m) |
| jerk | 1.000 000 X E +9 | joule (J) |
| joule/kilogram (J/kg) (radiation dose absorbed) | 1.000 000 | Gray (Gy) |
| kilotons | 4.183 | terajoules |
| kip (1000 lbf) | 4.448 222 X E +3 | newton (N) |
| kip/inch ² (ksi) | 6.894 757 X E +3 | kilo pascal (kPa) |
| ktap | 1.000 000 X E +2 | newton-second/m ² (N-s/m ²) |
| micron | 1.000 000 X E -6 | meter (m) |
| mil | 2.540 000 X E -5 | meter (m) |
| mile(international) | 1.609 344 X E +3 | meter (m) |
| ounce | 2.834 952 X E -2 | kilogram (kg) |
| pound-force (lbs avoirdupois) | 4.448 222 | newton (N) |
| pound-force inch | 1.129 848 X E -1 | newton-meter (N•m) |
| pound-force/inch | 1.751 268 X E +2 | newton/meter (N/m) |
| pound-force/foot ² | 4.788 026 X E -2 | kilo pascal (kPa) |
| pound-force/inch ² (psi) | 6.894 757 | kilo pascal (kPa) |
| pound-mass (lbm avoirdupois) | 4.535 924 X E -1 | kilogram (kg) |
| pound-force/foot ² (moment of inertia) | 4.214 011 X E -2 | kilogram-meter ² (kg•m ²) |
| pound-mass/foot ³ | 1.601 846 X E +1 | kilogram-meter ³ (kg•m ³) |
| rad (radiation dose absorbed) | 1.000 000 X E -2 | ** Gray (Gy) |
| roentgen | 2.579 760 X E -4 | coulomb/kilogram (C/kg) |
| shake | 1.000 000 X E -8 | second (s) |
| slug | 1.459 390 X E +1 | kilogram (kg) |
| torr (mm HG, 0°C) | 1.333 22 X E -1 | kilo pascal (kPa) |

* The becquerel (Bq) is the SI unit of radioactivity; 1Bq = 1 event/s.

** The Gray (GY) is the SI unit of absorbed radiation.

A more complete listing of conversions may be found in "Metric Practice Guide E 380-74,"
American Society for Testing and Materials.

Table of Contents

| Section | Page |
|---|------|
| Conversion Table | iii |
| Figures..... | v |
| Tables | viii |
| Acknowledgement | ix |
| 1 Summary | 1 |
| 2 Observations of T-Phase Transmission from the Ocean onto Land | 4 |
| 3 Far Inland T-Phases | 9 |
| 4 IMS Recordings of Small Explosion Sources..... | 13 |
| 5 Two-Dimensional Finite Difference Calculation of Propagation onto Land | 16 |
| 6 Discussion | 20 |
| 7 Numerical Modeling of T-Phases at IMS Stations | 23 |
| 8 Ascension Island Experiment..... | 27 |
| 9 Effect of Ocean Bottom Type on Long Range Hydroacoustic Propagation | 37 |
| 10 Conclusions and Recommendations | 41 |
| 11 References..... | 42 |
| Distribution List | DL-1 |

Figures

| Figure | | Page |
|--------|---|------|
| 1 | Hydroacoustic (H) and T-phase (T) stations in the future IMS network | 2 |
| 2 | Map of the Hawaiian Islands and surrounding ocean bottom bathymetry..... | 4 |
| 3 | Records from the June 30, 1997 Loihi event and station locations | 6 |
| 4 | Ratios of seismic spectra at stations in California that recorded the Loihi events, divided by the Point Sur spectra | 7 |
| 5 | T-phases recorded near the coast and far inland from the 1997 June 30 Loihi event. | 9 |
| 6 | Vertical and radial component seismograms from SAO for the 1997 June 30 event..... | 10 |
| 7 | T-phases were recorded far inland for the 1997/12/29 earthquake south of Australia..... | 11 |
| 8 | Map and bathymetry/topography for the path of T-phases from the earthquake of 1998/09/30 recorded at PLCA..... | 12 |
| 9 | Locations of 1997/11/10 events generating H-phases reported in the REB | 13 |
| 10 | H-phase arrivals associated with the two events at Point Sur, VIB and Wake Island..... | 14 |
| 11 | Spectrograms of one of the H-phase arrivals at Point Sur and VIB..... | 15 |
| 12 | Snapshot of the calculation at 65 seconds..... | 17 |
| 13 | Calculated horizontal velocity at a depth of 740 meters in water at the location of the Point Sur station and vertical and horizontal components of velocity on land close to the coast | 18 |
| 14 | Calculated spectral amplitudes of the horizontal velocity at a depth of 740 meters underwater and the vertical velocity at the surface on land near the coast | 19 |

Figures (Continued)

| Figure | Page |
|--------|--|
| 15 | Great circle path showing bathymetry to PSUR, RPV and VIB along the direction to Loihi from each station21 |
| 16 | Vertical velocity waveforms at a point on the surface 7 km inland from the coast for the three calculations with slopes of 10, 20 and 30 degrees.22 |
| 17 | Vertical component of velocity on the free surface for calculations with a low velocity surface layer and without22 |
| 18 | Bathymetry from the coastline to the starting point for each calculation23 |
| 19 | T-Phase conversion at the Tristan da Cunha IMS station is being modeled along profiles from the north and east24 |
| 20 | Bathymetry along the path to the IMS T-Phase station25 |
| 21 | Calculated Spectra in Water and on Land.....26 |
| 22 | Map of the Ascension Island along with the locations of the three MILS hydrophones and the two LCHEAPO units28 |
| 23 | Map of the Ascension Island itself showing the locations of the 10 LLNL seismic stations29 |
| 24 | 60-min spectrogram from ASCH 2330 |
| 25 | Time series and rms amplitude for the REB event recorded by the three MILS hydrophones and Maggie.....30 |
| 26 | Time series for the vertical components for 8 of the 10 seismic stations31 |
| 27 | Spectral ratios for the two events recorded by ASCH hydrophones 23 and 24.....32 |
| 28 | Ratio of the 23:45 event spectrum recorded by Lisa normalized by the uncalibrated spectra from ASCH 23 and 2434 |
| 29 | Transfer functions for 6 of the 10 stations35 |

Figures (Continued)

| Figure | | Page |
|--------|--|------|
| 30 | Normalized pressure field amplitude as a function of depth at 1000 km range Case 1 | 38 |
| 31 | Normalized pressure field amplitude as a function of depth at 1000 km range Case 2 | 38 |
| 32 | Normalized pressure field amplitude as a function of depth at 1000 km range Case 3 | 39 |
| 33 | Normalized pressure field amplitude as a function of depth at 1000 km range Case 4 | 39 |
| 34 | Normalized pressure field amplitude as a function of depth at 1000 km range Case 5 | 40 |

Tables

| Tables | | Page |
|--------|--|------|
| 1 | Origins of Loihi/Hawaii events used in this study | 4 |
| 2 | Velocity model for the California coast | 8 |
| 3 | Frequency Bands having Significant SNR for REB Event | 31 |
| 4 | Calibration Factors at 10 Hz for ASCH 23 and 24 | 33 |
| 5 | Bottom types used in this study | 37 |

Acknowledgement

We thank Marcia McLaren of Pacific Gas and Electric for the use of her data and for pointing out to us the large T-phases from the Loihi events.

Section 1 Summary

The objective of this project is to model propagation of T-phases from ocean to land using empirical and numerical methods, and to evaluate the expected performance of International Monitoring System (IMS) T-Phase stations. The empirical study uses data from pressure sensors in the ocean and coastal and island seismometers to measure the T-phase transfer function. The numerical study uses finite difference calculations to model T-phase propagation and conversion.

We model the T-Phase transition from ocean to land and corresponding evolution of the seismic signal. We model the transition with a composite technique using normal mode based numerical propagation codes to calculate the hydroacoustic pressure field in the ocean, and use this pressure field as input for the elastic finite difference code TRES to calculate the seismic propagation to land-based stations. Animations are created from the finite difference calculations to help visualize the complex conversion process. We have performed a detailed study of the transition from the Point Sur interim IMS station to seismic stations along the California coast. The numerical calculations are accurate to 9 Hz. We also perform numerical calculations for IMS stations VIB, Tristan da Cunha and Ascension Island.

An unusual result of the analysis that is observed both in the data and the calculations is that converted surface waves arrive at coastal stations earlier than body waves. This occurs because conversion to surface waves occurs farther offshore than conversion to body waves. For a typical coastal structure, the P-waves arrive in the middle of the surface wavetrain and are obscured at stations near the coast. T-phases propagate primarily as P-waves once they are well inland from the coast and the surface waves have been attenuated.

We have performed a number of test cases to assess the robustness of these results. Calculations for slopes varying from 10 degrees to 30 degrees show little difference in the results. Other studies have reported stronger effects for slopes steeper than 30 degrees. All of the IMS T-Phase stations, however, are located in areas where the offshore slope is less than 30 degrees. The California calculations have a low velocity surface layer, so we performed a set of calculations with the ocean embedded in a uniform structure. Again, the results are similar with coastal waveforms dominated by surface waves. In a faster, more uniform structure, however, the P-wave may appear ahead of the surface wave for slopes of 30 degrees or higher.

We perform an analysis of observed waveforms under water and on land recorded during the Ascension Island experiment. We find good agreement with the calculations, and better coupling than in the California coast observations, probably because of the close proximity of the stations to the coast.

We also look at the nature of T-phases after conversion from ocean to land by examining far inland T-phases. We find that T-phases propagate primarily as P-waves once they are well inland from the coast, and can be observed in some cases hundreds of kilometers inland. T-phase conversion attenuates higher frequencies, however we find that high frequency energy from underwater explosion sources can still be observed at T-phase stations.

Introduction.

The International Monitoring System (IMS) hydroacoustic network is a relatively sparse network consisting of 6 underwater hydroacoustic stations and 5 land-based seismic T-phase stations as shown in Figure 1. The hydroacoustic stations are much more sensitive to underwater signals than the T-phase stations and have a higher sampling rate and broader frequency range. The broader frequency range is important for identifying explosions, which are characterized by higher frequency content than other sources. Because of these limitations of T-phase stations, it is important to understand the efficiency of T-phase conversion in order to assess the capabilities of the IMS network for detection and identification of underwater sources.

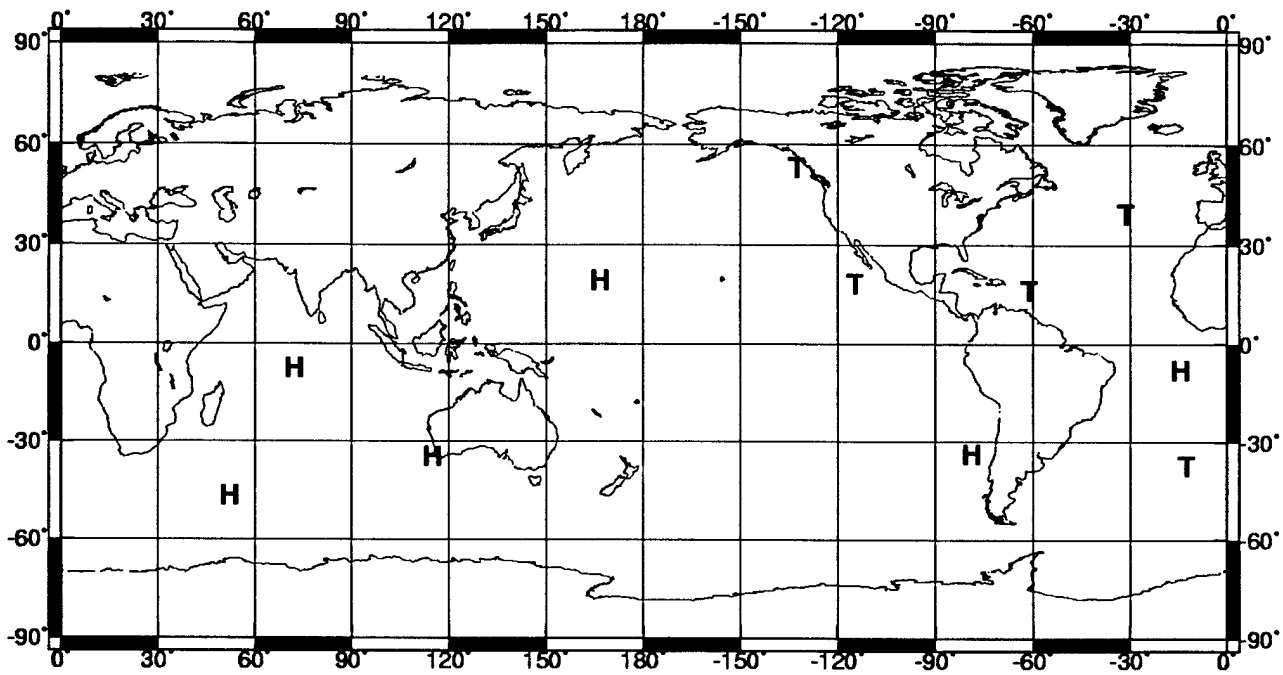


Figure 1. Hydroacoustic (H) and T-phase (T) stations in the future IMS network.

This is the final report on a three-year project to investigate these issues. The major topics covered in this research program are:

1. Empirical estimates of T-phase transfer functions using T-phases from earthquakes at Hawaii/Loihi recorded on the Point Sur hydroacoustic station and seismometers in the UC Berkeley and PG&E networks.
2. Numerical modeling of these T-phases, and analysis of the waveforms. A movie of one of the calculations is available on the Internet. Contact the authors for the current web address.

3. Analysis of H-phases from small explosions off the California coast observed at IMS stations.
4. Investigation of far inland T-phases observed at distances as great as 1000 km from the coast.
5. Modal decomposition of T-phases.
6. Empirical estimates of T-phase transfer functions using data from the Ascension Island experiment.
7. Numerical modeling of T-phases at IMS stations VIB, TRI, and Ascension Island.

Some of this work has previously been reported in Symposium papers (Stevens et al., 1998; Stevens et al., 1999; Stevens et al., 2000). This work is also described in two papers to be published in the special CTBT volume of Pure and Applied Geophysics (Stevens, et al, 2001; D'Spain et al, 2001). In addition, we have performed work under this contract on analysis of a large Russian hydroacoustic data set which we used to analyze the coupling of shallow explosion sources. This work has been presented in two Symposium papers (Eneva et al, 1999; Eneva et al, 2000) and in a third paper in the Pure and Applied Geophysics special issue (Eneva et al, 2001). The final results from this part of the project will be described in a separate final report.

Section 2

Observations of T-Phase Transmission from the Ocean onto Land

We gathered data sets from events that were recorded on both underwater and coastal seismic stations for the purpose of directly measuring T-phase conversion. Four earthquakes from the emerging seamount Loihi and on the island of Hawaii generated very strong T-phases that impacted the California coast. The location and size of these events, taken from the Reviewed Event Bulletin (REB) of the Prototype International Data Center, are listed in Table 1, and the locations are shown in the map in Figure 2.

Table 1. Origins of Loihi/Hawaii events used in this study.

| Event # | Origin ID | Date | Time (GMT) | Latitude | Longitude | m_b |
|---------|-----------|------------|------------|----------|-----------|-------|
| 1 | 751298 | 1996/07/23 | 13:24:59 | 18.9620 | -155.3959 | 4.40 |
| 2 | 752002 | 1996/07/24 | 17:38:50 | 18.9833 | -155.4213 | 4.51 |
| 3 | 1074833 | 1997/06/30 | 15:47:38 | 19.3108 | -155.1058 | 5.06 |
| 4 | 1110057 | 1997/08/15 | 01:54:38 | 19.4083 | -155.1098 | 4.43 |

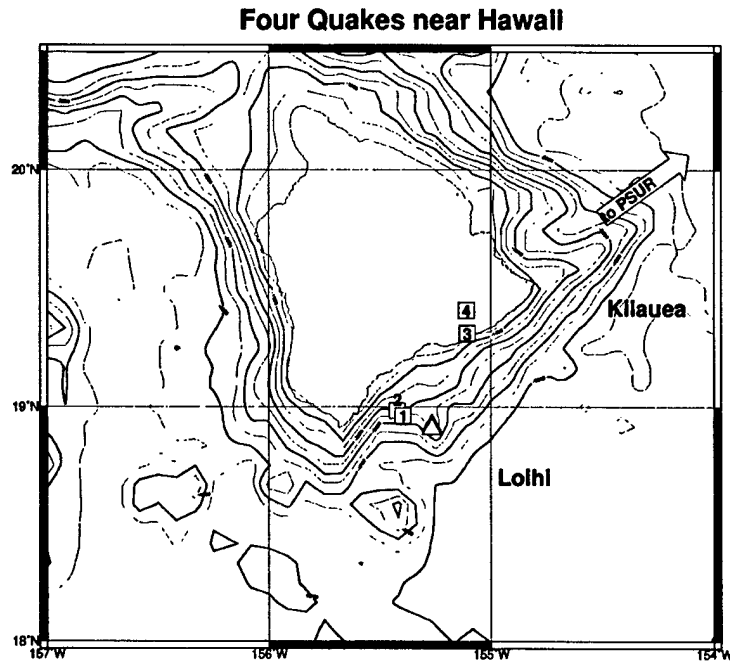


Figure 2. Map of the Hawaiian Islands and surrounding ocean bottom bathymetry. The squares labeled 1 through 4 (the square for event 2 is covered by that for event 1) show the epicentral locations of Hawaiian events 1 through 4 given in Table 1 as obtained from the Reviewed Event Bulletin. The two triangles (which are co-located on this spatial scale) show the corresponding epicentral locations for events 1 and 2 in 1996 derived from Hawaii Volcano Observatory local station recordings (Caplan-Auerbach, 1999). The bathymetry information, obtained from the GMT database (NOAA, 1998), are contoured in 500 meter increments.

We collected recordings of these events from the Point Sur (PSUR) hydroacoustic station, the Pacific Gas and Electric Central Coast seismic network (PG&E), and the Berkeley broadband digital seismic network (BDSN). The sampling rate and instrumentation are different for each of the three networks. Point Sur is sampled at 200 samples per second. A routine available from the PIDC converts the data to pressure in micropascals over a frequency band of approximately 3 Hz to 80 Hz. The routine also acts as a band pass filter, removing frequencies outside of this frequency band. From this, we determine the instrument response, which to a very good approximation is linearly proportional to frequency at frequencies less than 25 Hz. Data in the BDSN network is sampled at 20 samples per second. BDSN instrument responses were provided with the data, and are approximately flat to velocity in the 1-10 Hz frequency band. The PG&E network consists of S-13 seismometers with a sampling rate of 100 samples per second. The instrument at the PG&E stations is flat to velocity from 2 to 25 Hz, with a low pass filter above 25 Hz. We have gain corrections for each of the PG&E instruments, however we do not know the resulting units after the gain corrections are applied. We have made the assumption that the gains correct to 0.01 mm/sec because that makes the amplitudes consistent with the BDSN amplitudes, however any conclusions drawn from these measurements must take into account that the absolute amplitudes are uncertain. The IMS T-phase stations such as VIB also have S-13 seismometers and a sampling rate of 100 samples per second, however they do not have the low pass filter at 25 Hz. Because of the differences in instrumentation, the usable frequency band for obtaining T-phase transfer functions from this complete data set is about 2 to 9 Hz.

The location of these stations and the bathymetry of the California continental shelf are shown in Figure 3. This is a nearly optimal situation for study of T-phase conversion because the hydroacoustic waves impact the coastline almost perpendicular to the coast as shown by the ray path on Figure 3.

We calculated T-phase transfer functions for this data set by taking the ratio of the instrument corrected spectral amplitudes of the seismic stations to the Point Sur station for all good quality data at the PG&E stations and the 6 coastal BDSN stations (CMB was excluded because it is much farther inland). The spectral ratios were averaged for all events for each station. Two stations recorded all four events, 7 stations recorded 3, 9 stations recorded 2, and two stations recorded only 1 event. The resulting spectral ratios are shown in Figure 4. There is a clear decline in amplitude with frequency for both networks, but it is particularly pronounced for the BDSN network. This is likely due to greater attenuation of the higher frequencies because of the longer paths to the BDSN stations. Simulations discussed later in this paper indicate that much of the energy in the hydroacoustic wave is transmitted to land at approximately 200 m bathymetry, which corresponds to the contour line (Figure 3) nearest the coast. The crustal paths from the conversion point to the PG&E stations are only 5 to 20 km long, while paths to the BDSN stations are 40-75 km.

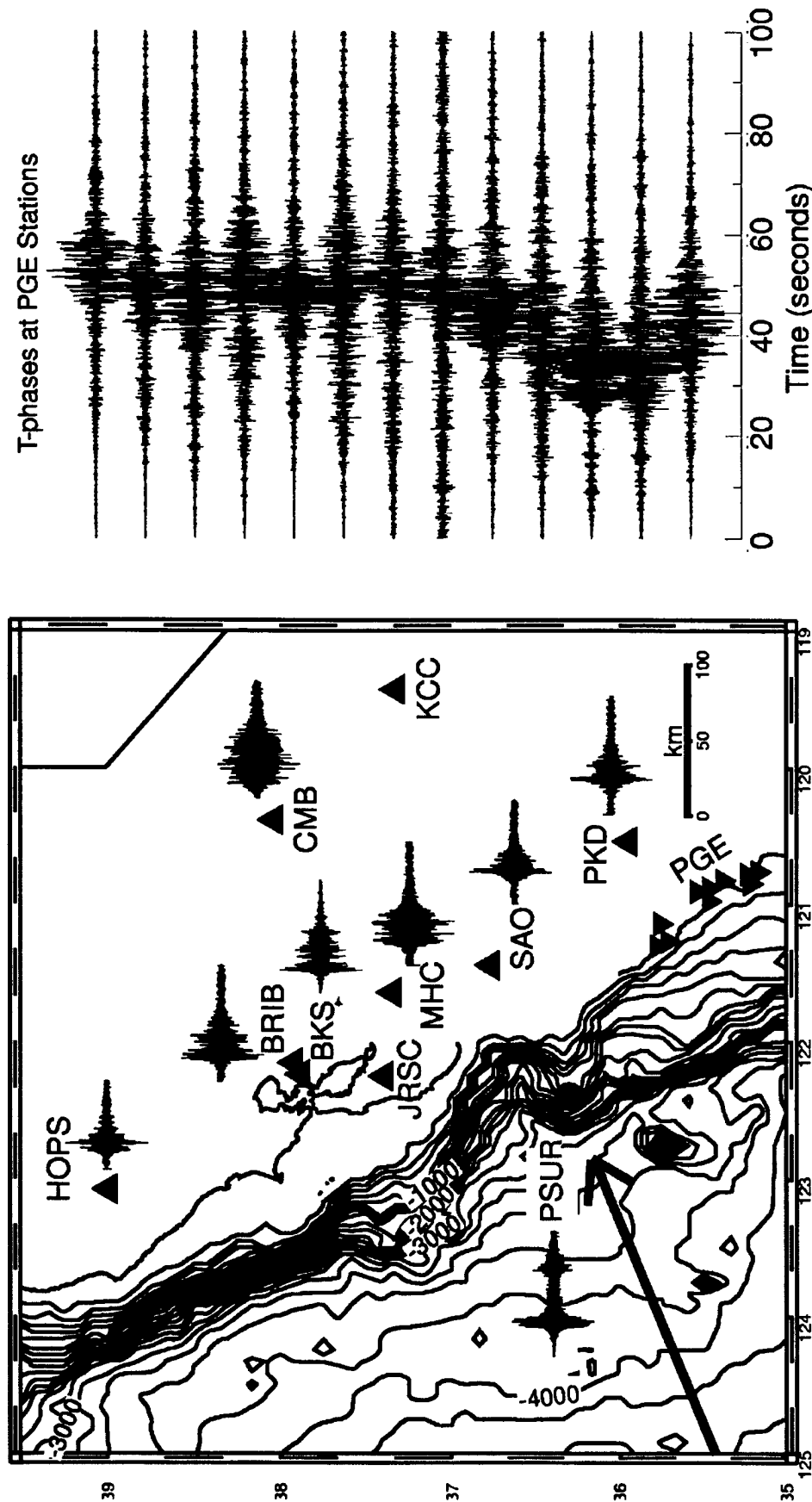


Figure 3. Records from the June 30, 1997 Loihi event and station locations. The propagation direction is indicated by the arrow, which points to the hydroacoustic station PSUR (indicated by the circle). 150 seconds of the T-phase record is shown to the station's left. The BDSN stations (large triangles) and corresponding records are included on the map on the same scale. The PG&E station locations are indicated by inverted triangles and their waveforms are shown to the right, in order of increasing distance from bottom to top. The arrival times do not correspond well to total distance because the distance from the conversion point varies. The bathymetry is contoured in 200 meter intervals.

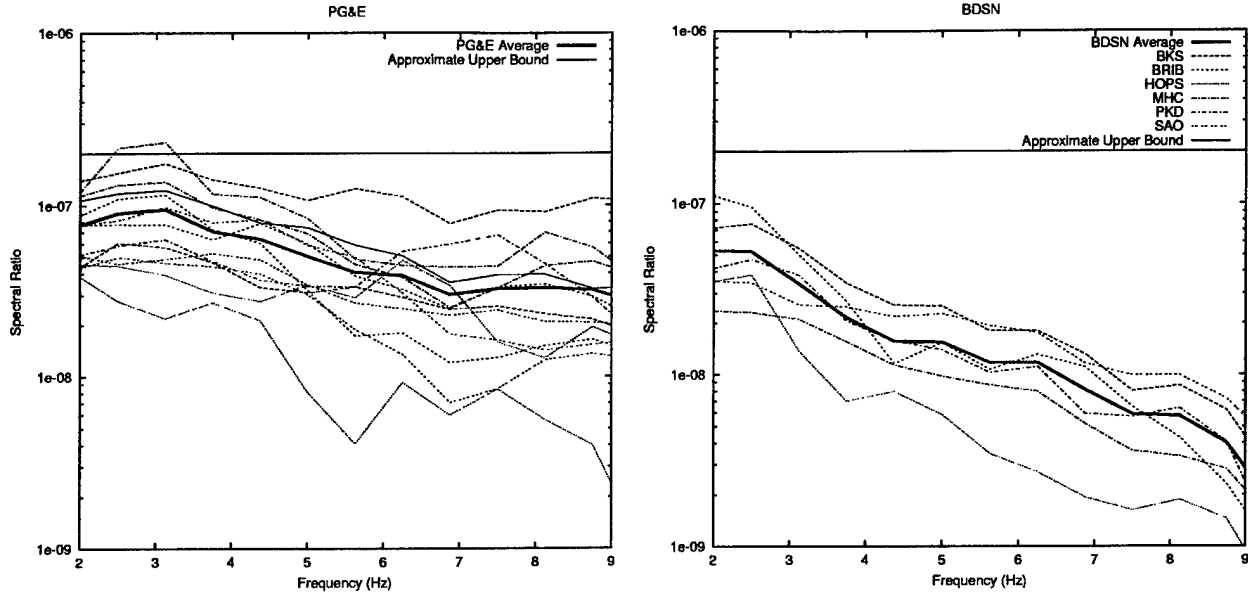


Figure 4. Ratios of seismic spectra at stations in California that recorded the Loihi events, divided by the Point Sur spectra. These are T-phase transfer functions converting pressure to vertical velocity. The frequency band shown here is from 2 to 9 Hz. The left plot shows PG&E stations and the right plot shows BDSN stations. The absolute amplitude of the PG&E records is uncertain, however the amplitude of the BDSN records, and the spectral shape of both sets of curves, are accurate. Also shown is the approximate upper bound for conversion from pressure in the ocean to particle velocity on land. The heavy line is the average log spectral ratio for all stations except far inland stations. Spectral ratios are in MKS units (meters/second/Pascal).

Also shown in Figure 4 is an approximate upper bound on the transfer function derived from the simple case of a plane acoustic wave travelling in the ocean and propagating into a solid at normal incidence. This is an approximate upper bound in the sense that any scattering or other boundary effects will reduce the amplitude below this level, although conversion to shear waves or focusing could cause amplitudes to exceed this value. For a plane acoustic wave, the pressure is related to the velocity at a point by $P = \rho \alpha V$ where α is compressional velocity, ρ is density and V is particle velocity in the direction of propagation. For propagation of a plane wave at normal incidence from a fluid into a solid, the reflection coefficient R and transmission coefficient T for velocity are given by (e.g. Achenbach, 1973):

$$R = \frac{\rho_s \alpha_s - \rho_f \alpha_f}{\rho_s \alpha_s + \rho_f \alpha_f} \quad (2.1)$$

$$T = \frac{2 \rho_f \alpha_f}{\rho_s \alpha_s + \rho_f \alpha_f} \quad (2.2)$$

where the subscript s indicates solid and f indicates fluid. The transmission coefficient for propagation of pressure in the fluid to velocity in the solid is therefore:

$$T_{p \rightarrow v} = \frac{2}{\rho_s \alpha_s + \rho_f \alpha_f} \quad (2.3)$$

Table 2 lists a velocity model for the California coast near Point Sur from Mooney et al (1998) with the shear velocity as modified by Stevens and McLaughlin (1997). Using a typical water velocity and density of 1480 m/s and 1000 kg/m³, respectively, we can estimate upper bounds on the velocity transfer function of 0.21 and 0.36 for the top two layers of the coastal California earth model. The pressure to velocity transfer function for each layer has an upper bound of 1.4×10^{-7} and 2.4×10^{-7} meters/second/Pascal. The heavy lines in Figure 4 show the average transfer function for all of the coastal stations in the BDSN and PG&E networks. At 2 Hz, the BDSN spectra are a factor of 3-4 less than the estimate given above, which gives a numerical estimate of the efficiency of T-phase transmission into the coast. That is, the BDSN records show that at low frequencies the transfer function is reduced by complex coastal interactions by a maximum of a factor of 3-4. The spectra of the BDSN records fall off by an order of magnitude over the 2-9 Hz frequency band. The PG&E records show that for stations close to the coast, the maximum attenuation with frequency is a factor of 3-4 over the 2-9 Hz frequency band.

Table 2. Velocity model for the California coast.

| DEPTH (M) | P VELOCITY (M/S) | S VELOCITY (M/S) | DENSITY (KG/M³) |
|------------------|-----------------------------|-----------------------------|---------------------------------------|
| 500 | 3400 | 1500 | 2200 |
| 1500 | 5000 | 2900 | 2500 |
| 11000 | 6100 | 3484 | 2750 |
| 21000 | 6300 | 3503 | 2800 |
| 31000 | 6600 | 3464 | 2900 |
| ∞ | 8000 | 4260 | 3300 |

Section 3 Far Inland T-Phases

The ocean hydroacoustic phase may convert to a variety of complex phases due to the interaction with the coast. We can get some insight into the type of conversion that occurs by looking at far inland T-phases, and examining the propagation speeds of these waves. The T-phase from the 1997/06/30 event is large enough to be seen well inland from the California coast. Figure 5 shows two sets of seismograms recorded along the two (approximate) great circle paths. The paths are from SAO to KCC and from JRSC to MHC to CMB. Since the waveform is dispersed, there is some uncertainty about when to pick the arrival, however if we use the peaks of each wave train, then we get a velocity between SAO and KCC of 6.8 km/sec, and a velocity along the path of the other three stations of 5.6 km/sec. These velocities correspond to P-wave speeds, so the T-phases must be travelling as P-waves over this range.

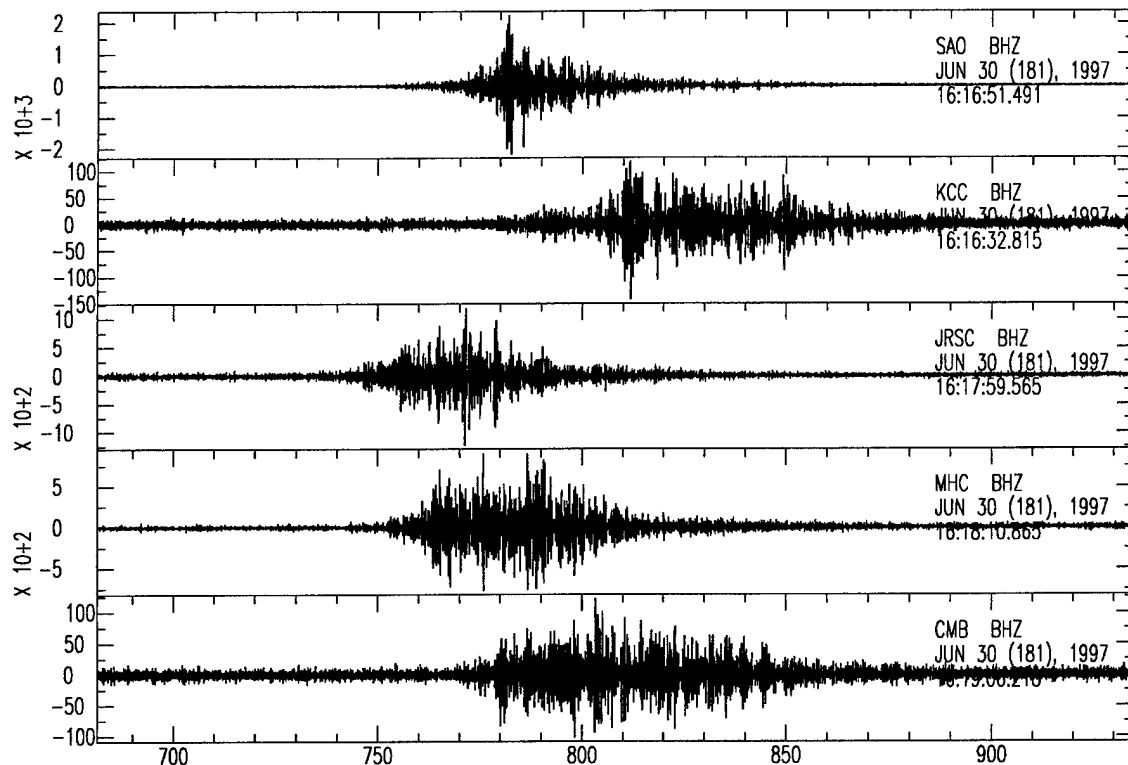


Figure 5. T-phases recorded near the coast and far inland from the 1997 June 30 Loihi event. The top two seismograms and the bottom three seismograms were recorded at stations along approximately the same great circle path. The horizontal axis is time in seconds. The data has been high pass filtered at 2 Hz.

Particle motion provides an independent means of assessing wave type. Figure 6 shows that the particle motion for the largest part of the record, near the front of the T-phase, is strongly linear. This part of the record is clearly dominated by body waves, most likely P-waves, in agreement with the conclusion from travel times. Linearity decreases later in the record, although it's not

clear whether that is due to the arrival of later scattered P-wave energy, surface wave arrivals, or a mixture of phases. The particle motion of the earliest part of the T-phase is elliptical and retrograde, suggesting that this part of the wave train is composed of Rayleigh waves. This is consistent with the simulations later in this paper, which indicate that surface waves can precede the P-wave near the coast, due to earlier conversion of the T-phase in water to surface waves.

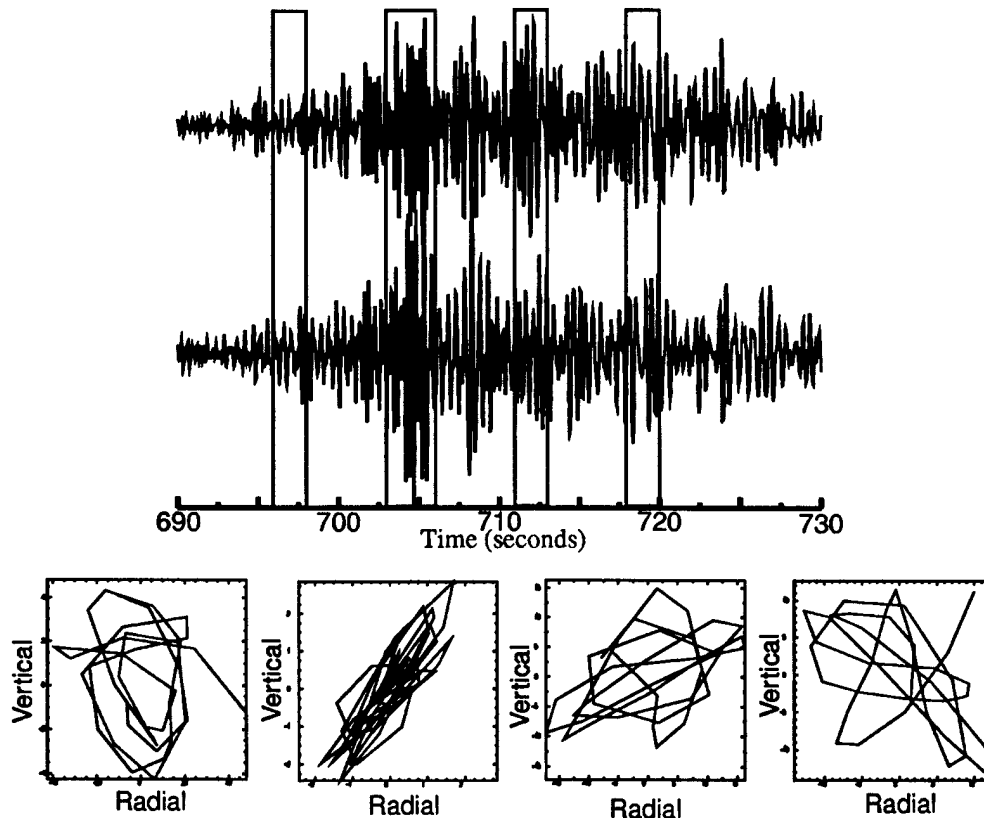


Figure 6. Vertical (top trace) and radial (lower trace) component seismograms from SAO for the 1997 June 30 event. Particle motions for four outlined time windows are shown below the seismograms. The very linear motion of the second time window indicates dominance there by body waves, and the elliptical motion of the first time window suggests that the early part of the wave train is composed of surface waves.

Cook and Stevens (1998) collected a number of examples of T-phases recorded far inland from the coast. We show two examples of these here. In Figure 7, we show the locations of stations that recorded T-phases from an earthquake south of Australia, and the bathymetry and topography along the path. The path on land to the most distant station, ASPA, is more than 1000 km long. The travel times for all records are consistent with propagation on land at Pn velocity. The velocity labeled “AV” on the bathymetry plot is the apparent velocity in the water after subtracting the travel time for propagation on land. This apparent velocity acts as a consistency check and should be close to the velocity of water if the T-phase is traveling on land at Pn speeds. This is additional evidence that T-phase propagation on land, at least once the wave has propagated well inland from the coast, consists of P-waves.

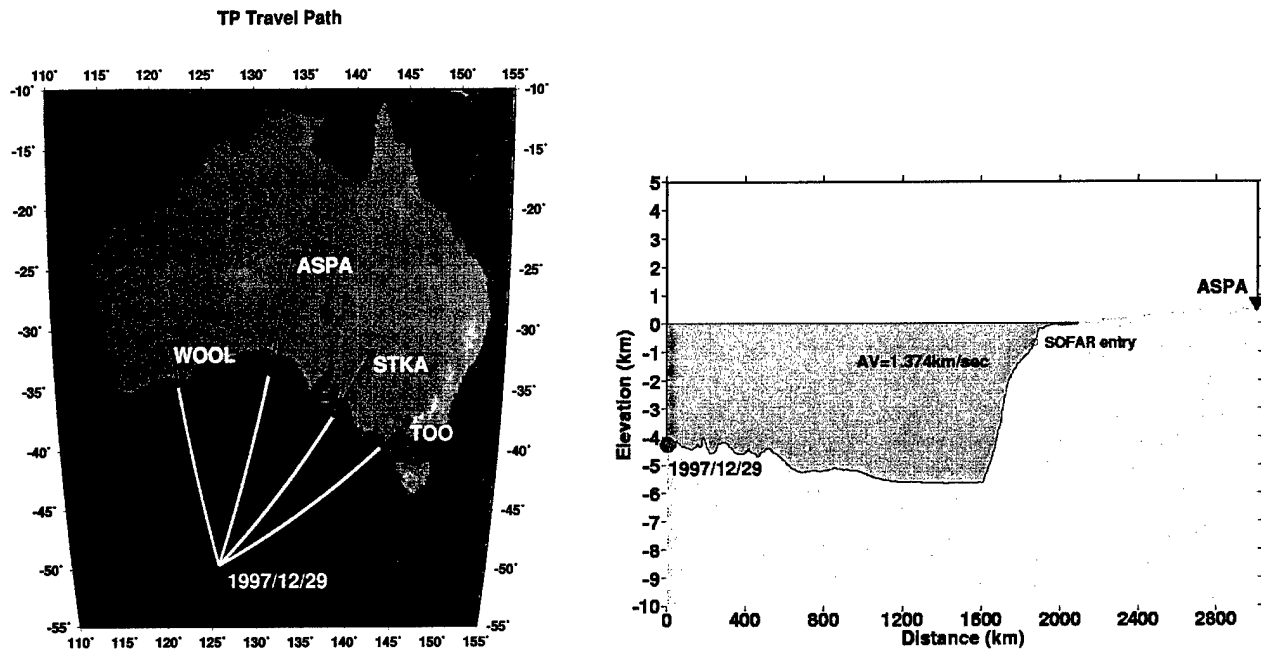


Figure 7. T-phases were recorded far inland for the 1997/12/29 earthquake south of Australia. The left hand figure shows a map of the source to receiver paths, and the right hand figure shows bathymetry and topography along the path. The circle next to the date is the epicentral location.

Figure 8 shows a second example, this time of a T-phase from an earthquake in the eastern South Pacific Ocean recorded in Argentina, on a path that traveled through the Andes and over a distance of approximately 300 km on land. Far inland T-phases have very peculiar travel times because they travel very slowly (~ 1.4 km/s) in the ocean, and very fast (up to 8 km/sec) as P-waves on land. Consequently, the T-phase starts out far behind the other seismic phases, but will eventually catch up to the Rayleigh wave if it travels far enough. Because of this, there is some danger in a semi-automated processing system like the IDC that T-phases could be misidentified as other phases. One approach to solving this problem would be to calculate the T-phase travel time for each event and if it is found, to associate the T-phase with the correct event.

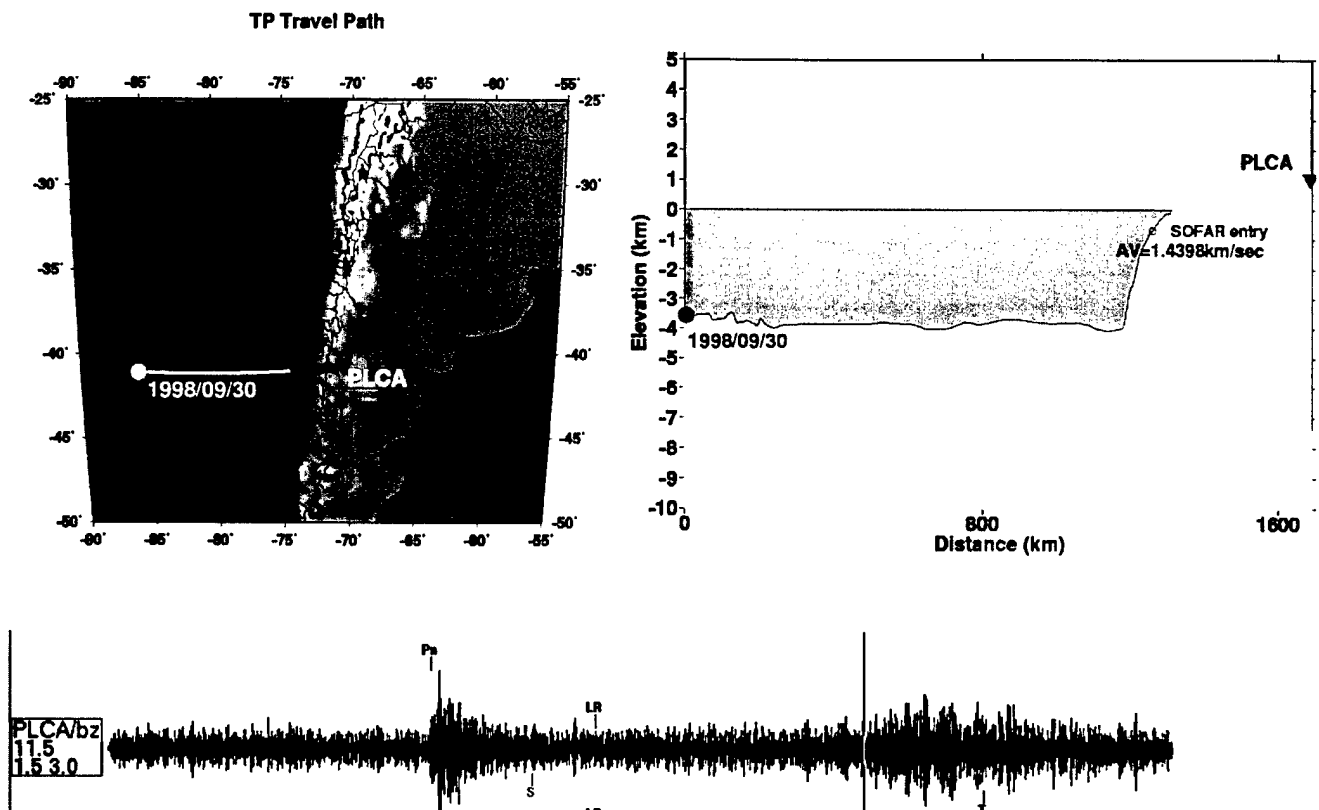


Figure 8. Map (left) and bathymetry/topography (right) for the path of T-phases from the earthquake of 1998/09/30 recorded at PLCA. At the bottom is the seismogram recorded at PLCA showing with the phases marked.

Section 4

IMS Recordings of Small Explosion Sources

On November 10, 1997, 20 “H-phases” were reported in the Reviewed Event Bulletin. “H-phases” refer to T-phases which have the characteristics of explosions – short duration and enhanced high frequencies. These arrivals came from events that were located off the coast of San Francisco as shown on the map in Figure 9.

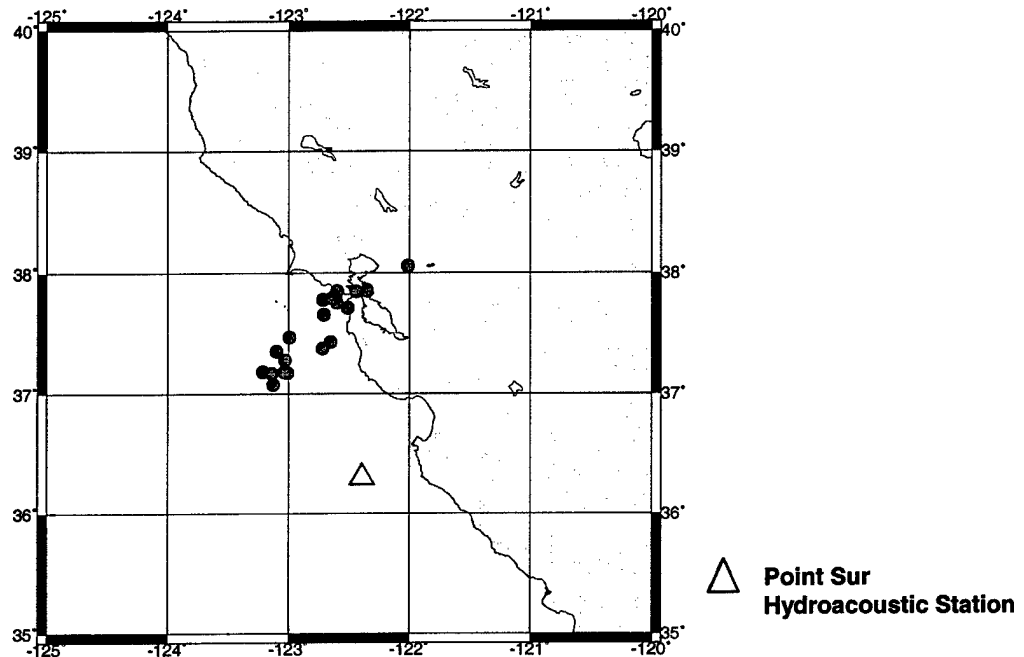


Figure 9. Locations of 1997/11/10 events generating H-phases reported in the REB.

These H-phases were observed not only at Point Sur but also at Wake Island, nearly 10,000 km away, and at VIB, the T-phase station in Canada (see Figure 1). These arrivals were subsequently identified as originating from a series of explosions detonated off the coast of California as part of a submarine detection exercise. There were a total of 60 explosions detonated, all identical and consisting of four pounds of C4 explosive. This provides an interesting test case for the detection, location, and identification capabilities of the IMS. First, the IMS and the processing done at the PIDC did very well in being able to detect and identify as explosions these very small tests. Second, the ability to see and identify these events at Wake Island shows just how well these signals travel in the ocean on unobstructed paths. Third, if a four pound explosion can be seen this easily, an explosion in the ocean at the one kiloton design threshold of the IMS should be impossible to miss unless there are severe path obstructions (Oliver and Ewing, 1958, reported that the T-phase from the 30 kiloton underwater explosion Wigwam was large enough to be felt in California and Hawaii). However, as is apparent from Figure 9, locating small events is a more difficult problem. The PIDC event locations were distributed over a wide arc, with some events actually located on land. Although we do not know the exact location of the explosions, there are clearly some large location errors.

1997 Nov 10 Prototype IDC REB Event Showing Correlatable Waveform Characteristics

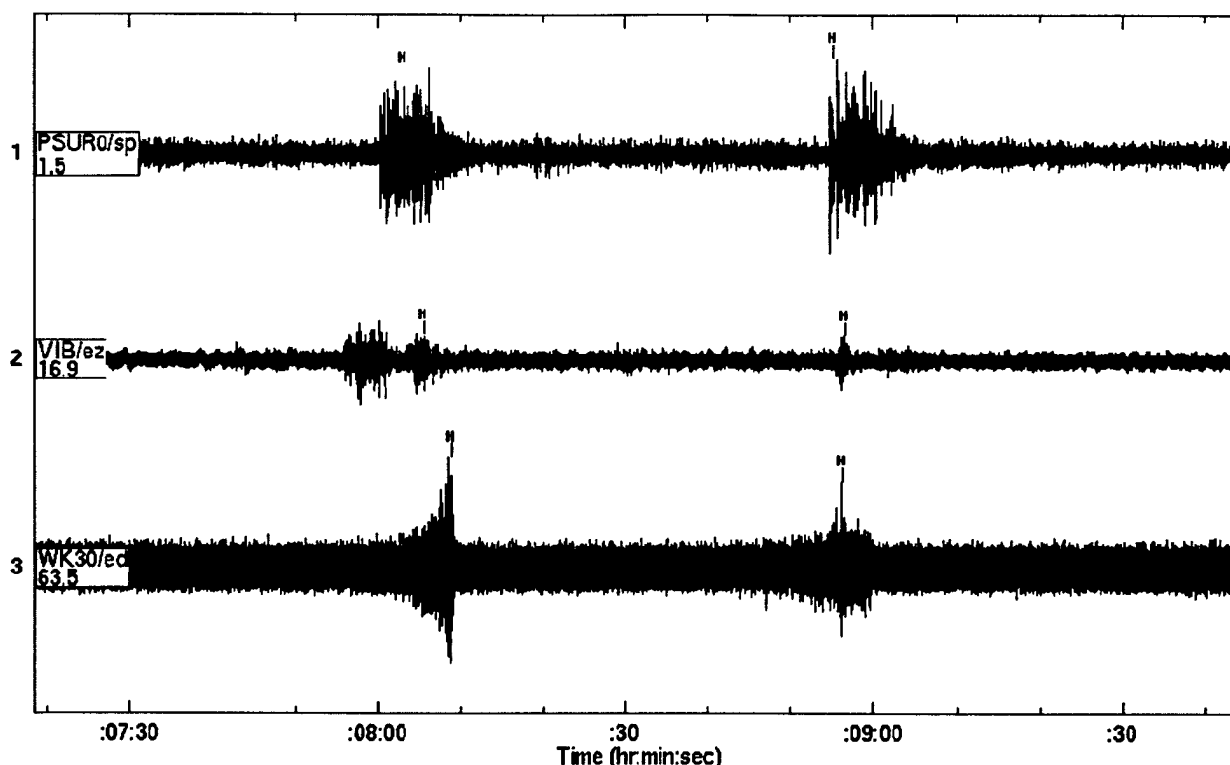


Figure 10. H-phase arrivals associated with the two events at Point Sur (top), VIB (middle) and Wake Island (bottom). "H" marks the arrival times listed in the REB. The time shown is the time after 1997/11/10 10:20 at PSUR. VIB and WAKE are advanced by the predicted travel time relative to PSUR. The absolute times of the first marked H in each trace is 10:28:03 (PSUR), 10:47:16 (VIB), and 11:45:35 (WAKE). Although the arrivals at VIB are less distinct than the other stations, the consistency with the arrival times of the signals from multiple events at the other two stations makes it unlikely that they have been misidentified.

Figure 10 shows arrivals from two of the explosions recorded at the three IMS stations. The character of the waveforms is distinctly different at each station. Wake, in particular, is much more emergent, and has a maximum at the end of the wave train. These events also provide an interesting test of whether the high frequencies characteristic of explosion sources can be observed at T-phase stations. Figure 11 shows spectrograms of two waveforms, one recorded at Point Sur and one at VIB. The spectrogram at Point Sur is exactly what is expected from an explosion: short duration and strong high frequency energy, extending across the entire pass band of the instrument to near 90 Hz. The VIB spectrogram also shows strong high frequency energy extending across the pass band of the instrument to about 40 Hz. This shows that, for this example and similar cases, waveforms from explosions in the water will contain enough high frequency energy after propagation to T-phase stations to identify them as explosions.

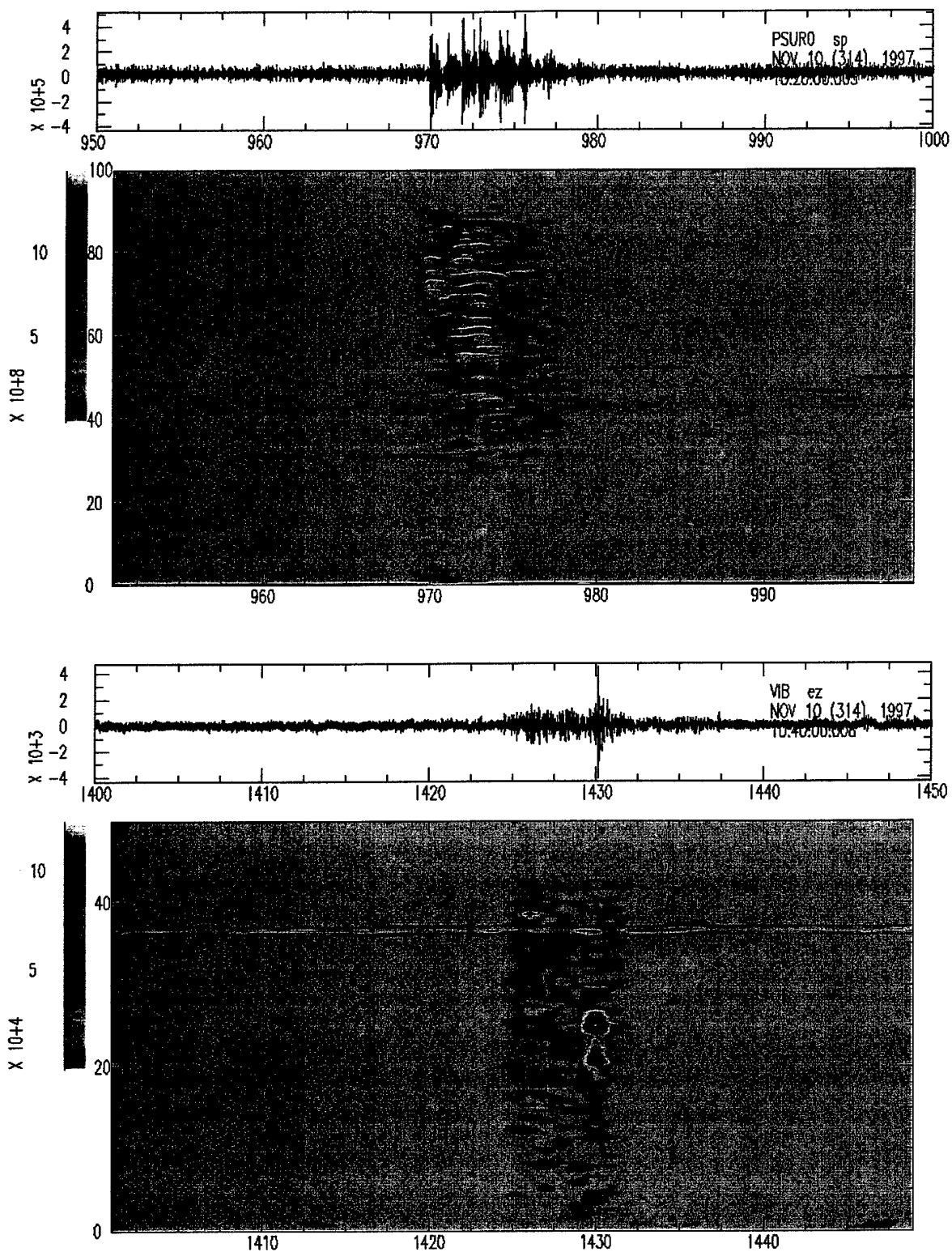


Figure 11. Spectrograms of one of the H-phase arrivals at Point Sur (top) and VIB (bottom). Both stations show the strong high frequencies characteristic of underwater explosions. The horizontal axis is time in seconds.

Section 5

Two-Dimensional Finite Difference Calculation of Propagation onto Land

We use the two-dimensional finite difference code TRES2D to model the propagation of hydroacoustic waves onto the coast. TRES is a finite difference code developed at Maxwell Technologies (formerly S-Cubed) with 2D and 3D versions that are used to model wave propagation. In this case we model a 2D slice of the propagation path. The normal mode code Kraken was used to calculate the acoustic wave field in the ocean at a distance of 3710 km from Loihi (Kraken can be obtained through the Ocean Acoustics Library web site at <http://oalib.njit.edu/>). This solution was used as the source in the finite difference calculation using the representation theorem (see Stevens et al, 2001 for implementation details). Even though this is a two-dimensional problem, it requires a very large calculation because the distances of interest are large, about 100 km, the wave speed in the water is slow, and we are interested in frequencies higher than 1 Hz. We used recursive grid refinement (McLaughlin and Day, 1994), with the top 5 km portion (including ocean and the upper oceanic crust) covered with uniform grid cells of 16.75m x 16.75m and the remaining grid with cells of 67m x 67m. The calculation is accurate to 9 Hz throughout all the grids and the simulation time is 100 seconds. The time step is 0.005s for 67m spacing and 0.00125s for 16.75m spacing.

Velocities for the full grid were saved for each second of time in the calculation, and these were used to create images and animations of the velocity fields to help visualize the evolution of the velocity field. There is a gradual decay of the hydroacoustic wave as it travels upslope, with body waves emitted continuously with varying amplitudes into the earth below, and a surface wave that gradually forms along the ocean bottom. At sharper bathymetric gradients the transmission is increased, and when the hydroacoustic wave reaches an ocean depth of 200 meters, there is a burst of body-wave energy much larger than anywhere else along the path. Strong surface waves are generated on land from the edge of the ocean to the boundary of the calculation. Figure 12 shows a snapshot of the horizontal displacement field at 65 seconds. The figure shows the burst of energy at 200 meter depth. Color animations of this calculation can be viewed online (contact authors for web address). The calculated T-phases have some very odd properties. As can be seen in Figure 12, a strong surface wave develops quite early and can be seen on land at 65 seconds, which is the same time that the burst of body waves occurs. Consequently the surface wave appears in the wave train before, and simultaneous with, the body waves generated by the final decay of the hydroacoustic wave. The T-phase near the coast is therefore a mixture of seismic phases.

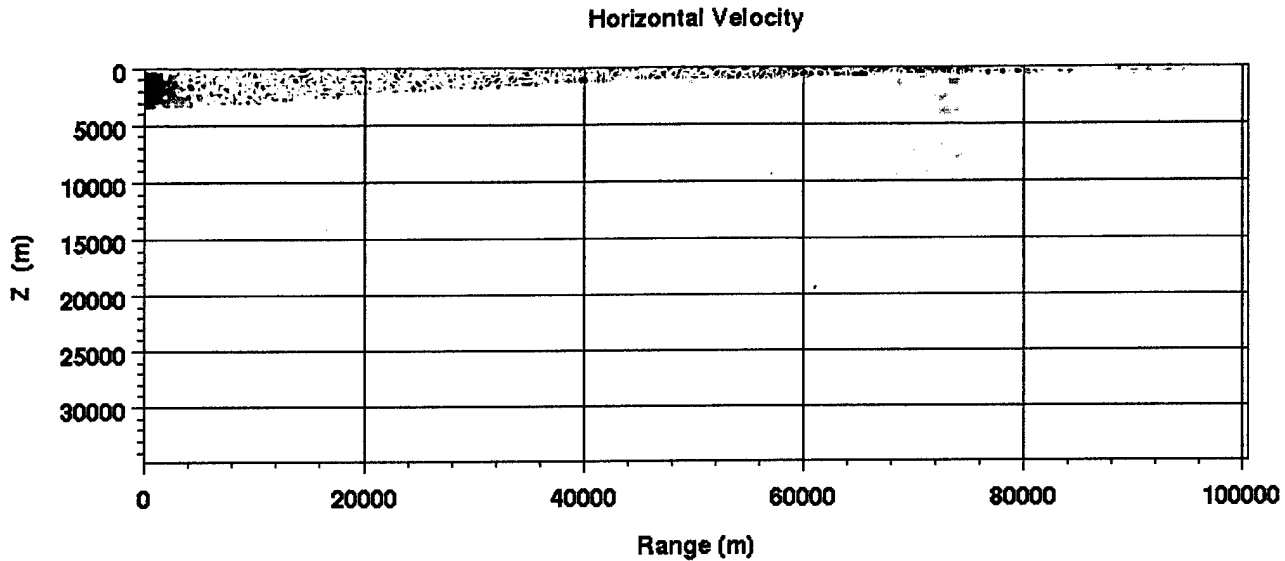


Figure 12. Snapshot of the calculation at 65 seconds. The dominant hydroacoustic arrival has reached a depth of 200 meters. At this point there is a burst of energy transferred as body waves from the ocean into land. Zero range corresponds to the point 3710 km from Loihi. The ocean/land interface at the surface is at location 87368.

The results of the calculation were saved with a much finer time resolution at selected locations along the surface, and at a depth of 740 meters in the center of the sound channel. Figure 13 shows the calculated horizontal velocity in the water at 47235 m, which corresponds approximately to the location of the Point Sur hydroacoustic station. (Zero range corresponds to the point 3710 km from Loihi). Also shown are the horizontal and vertical components of the waveform on the surface at location 87904 m, which is on land close to the coast. The amplitude ratios between the velocity on land and in the water are about 0.2, which is consistent with our earlier estimates of the upper bound of the transfer function (note the earlier discussion was for pressure to velocity which adds a factor of about 10^{-7}). The waveforms on land are complex and longer in duration than the underwater waveform. From travel times and particle motion it is clear that the dominant energy is traveling at surface wave speeds. The complexity of the waveforms arises from the complex way the waves are generated over an extended region of the ocean bottom.

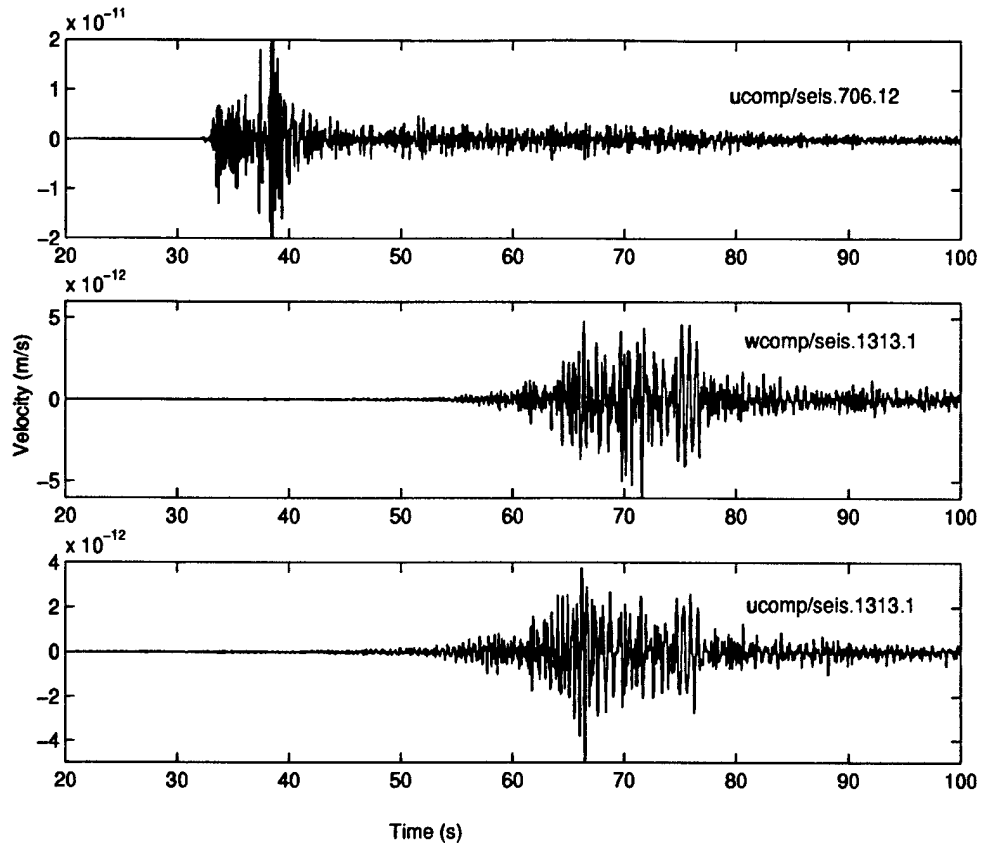


Figure 13. Calculated horizontal velocity at a depth of 740 meters in water at the location of the Point Sur station (top) and vertical (mid) and horizontal (bottom) components of the velocity on land close to the coast. The horizontal axis is time in seconds since the start of the calculation.

Figure 14 shows the spectral amplitude of the horizontal velocity in the 1-9 Hz frequency band underwater at the Point Sur location and the vertical velocity at a station on land close to the coast. The underwater spectrum is nearly flat across this frequency band. The spectra on land, however, exhibit a significant decline in amplitude with frequency, similar to the spectral decline observed for the coastal California stations. This suggests that during transmission from water to land, the higher frequencies scatter more strongly than the lower frequencies, leading to a decline in high frequency content in the coastal waveforms.

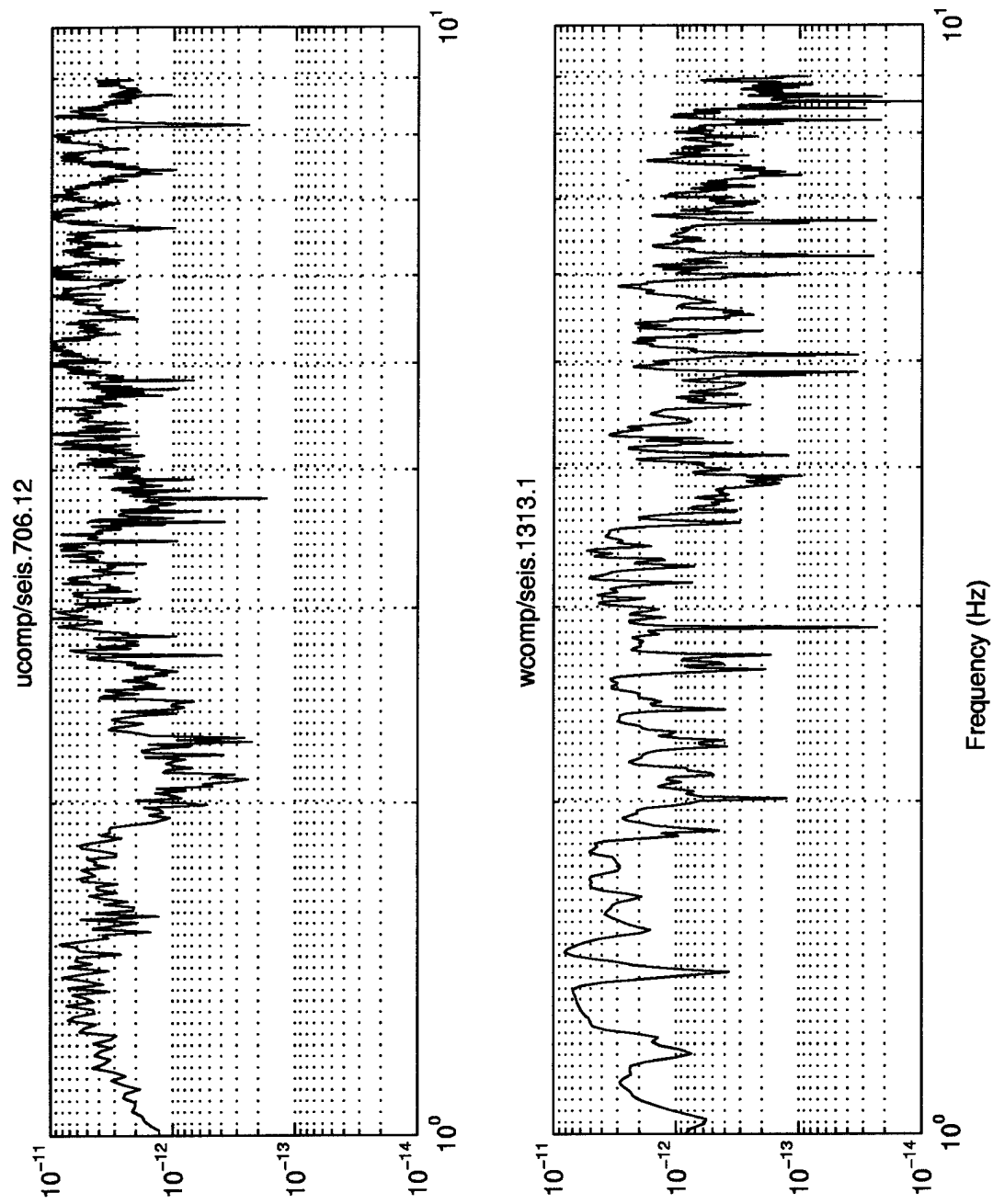


Figure 14. Calculated spectral amplitudes of the horizontal velocity at a depth of 740 meters underwater (top) and the vertical velocity at the surface on land near the coast (bottom).

Section 6

Discussion

We have used T-phase observations in water and on land together with numerical calculations of T-phase propagation from water to land in order to understand the nature of T-phase conversion. The results are complex and at first glance contradictory. Whereas T-phases are observed to travel at P-wave speeds on land, the calculations show strong surface waves near the coast. However, the calculations also show lower amplitude body wave arrivals even very close to the coast, and strong body waves propagated away from conversion points along the ocean bottom. Some of this body wave energy will return farther inland as P_g and P_n phases. The high frequency surface waves, on the other hand, can be expected to attenuate away very quickly and will not propagate to large distances. We therefore expect to see stronger surface waves than P-wave arrivals near the coast, with the surface waves dying out and the P-waves becoming dominant as the wave travels inland.

A similar study was performed by Piserchia et al (1998), in which they modeled T-phase conversion from an explosive source in the ocean, observed on the islands of Mururoa and Fangataufa in the South Pacific Ocean. They used ray tracing instead of a modal solution, and calculated Green's functions along a vertical boundary in order to propagate the source onto the islands. They found that the T-phase on land consisted of two P waves followed by two Rayleigh waves, where the multiple arrivals are identified as coming from different conversion points. The calculation was performed for a dominant frequency of 6 Hz, and in this case the calculated P and Rayleigh waves were found to be comparable in size. Cansi and Bethoux (1985) modeled far inland T-phases as converted T-P and T-S phases along a curve corresponding to a fixed depth in the ocean. They found good agreement with observed waveforms with synthetics composed only of P and S waves. Talandier and Okal (1998) studied conversion of T-phases on steep island slopes using data from the Polynesian Seismic Network and found from the observations and ray tracing arguments that the T-phase consisted primarily of P-waves at distances greater than 9 km from the conversion point. At closer distances, they found that the T-phase was more complex and composed primarily of S-waves and surface waves. They also suggested that only surface wave conversion would occur for slopes with angles of less than 16 degrees.

Great Circle Path Bathymetry PSUR, VIB, BKS & RPV to Loihi

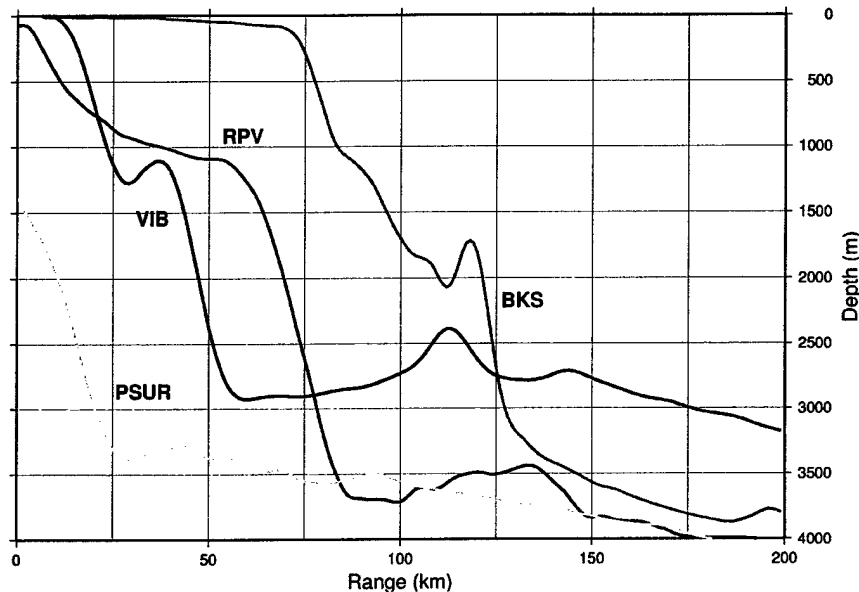


Figure 15. Great circle path showing bathymetry to PSUR, RPV, BKS, and VIB along the direction to Loihi from each station. Zero range corresponds to the station location. Vertical exaggeration makes the slopes appear steeper.

We have modeled propagation onto the California coast in considerable detail because of the availability of a good data set for comparison, with stations both underwater and on land. The question arises as to how closely this models propagation onto the IMS T-phase stations which have different bathymetric profiles. Also, we would like to know how sensitive the calculations are to the details of the profile, and in particular to the slope of the ocean bottom on the approach to the coast. Figure 15 shows the bathymetric profiles off the coast of California in the direction of Loihi passing through the Point Sur, RPV, and BKS stations. Also shown for comparison is the profile in the direction of Loihi off the coast of VIB. Although they differ in detail, the structures are comparable in general features. The slope off the coast of VIB is similar to the slope off of BKS, although VIB is much closer to the coast. The slope through RPV is smaller. The slope used in the calculations is intermediate between these slopes. Note that there is considerable vertical exaggeration in these figures. Even the steepest part of the slope at VIB decreases by 1000 meters over a distance of 10 km, which corresponds to an angle of about 6 degrees. The steepest slopes off of the island T-phase stations change by 1000 meters over a distance of four km, an angle of about 14 degrees. To assess how much difference this caused, we ran three additional finite difference calculations, using the same ocean structure and modes as in the calculations above, but with constant slopes of 10, 20, and 30 degrees. In each case, the coastal boundary was fixed at 80 km from the left edge of the grid. The resulting vertical displacements at a point 7 km inland from the coast are shown in Figure 16. The waveforms are remarkably similar to each other and to the earlier calculations. The waveforms consist primarily of surface waves of comparable amplitude. The main difference is in the timing of the body wave which close examination shows arrives earlier than the surface wave for the 30 degree slope, and is within the surface wave wavetrain for the shallower slopes.

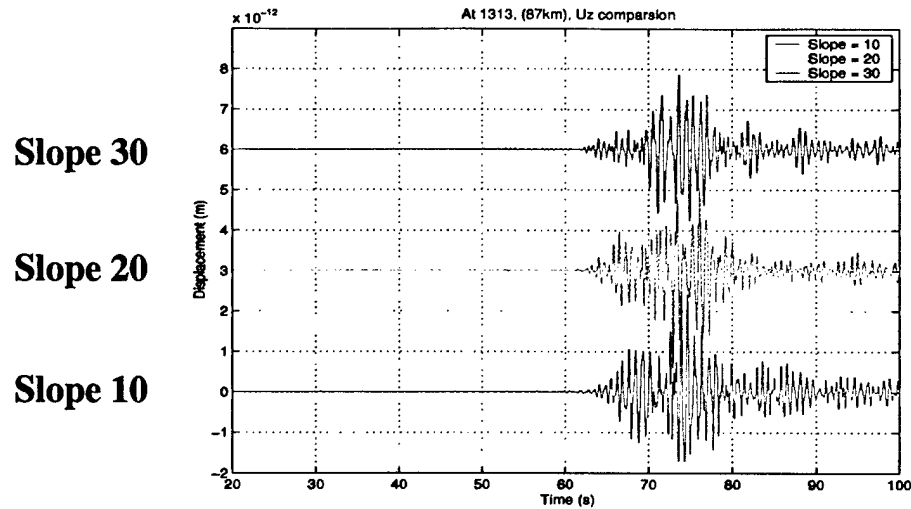


Figure 16. Vertical velocity waveforms at a point on the surface 7 km inland from the coast for the three calculations with slopes of 10 (bottom), 20 (middle), and 30 (top) degrees.

One of the conclusions that can be drawn from the calculations is that T-phases observed close to the conversion point should be dominated by surface waves. The calculations discussed above all had a low velocity layer near the surface, which could amplify the surface waves. To assess the magnitude of this effect, we performed another calculation with a uniform structure. The ocean was modeled as having a depth of 3500 meters and then a slope of 30 degrees up to the coast. Figure 17 shows the vertical component of velocity at a point 7 km from the coast for the two calculations with the uniform structure and the full structure including the low velocity layer. As expected, surface waves are smaller, however the wavetrain is still dominated by the surface waves which are much larger than the body waves at this distance. Body waves arrive at about 62 seconds. They are difficult to see, but can be identified by their particle motion.

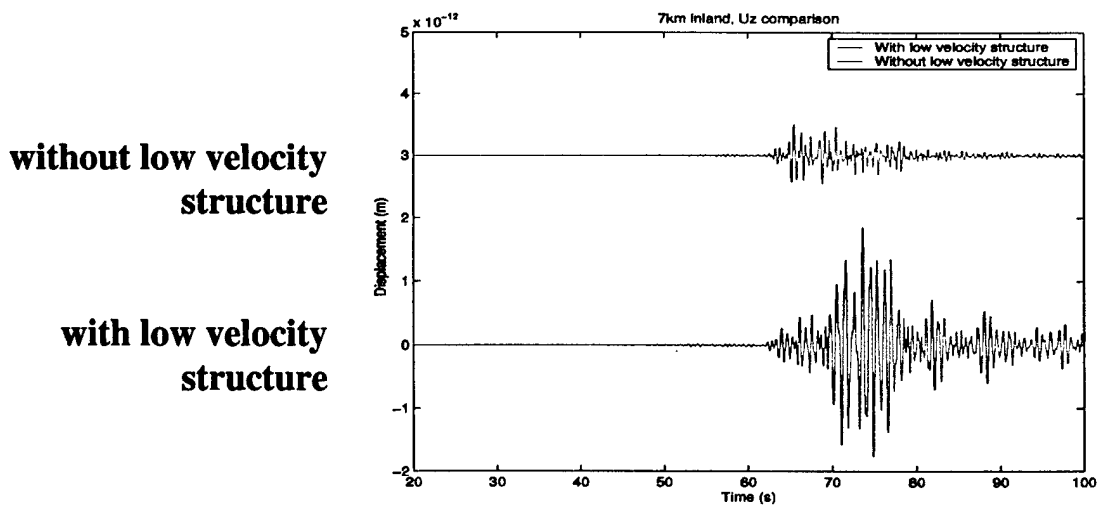


Figure 17. Vertical component of velocity on the free surface for calculations with a low velocity surface layer (bottom) and without (top).

Section 7

Numerical Modeling of T-Phases at IMS Stations

In order to better assess the T-Phase conversion at IMS stations, two-dimensional finite difference calculations were performed for the actual bathymetric profiles for two of the IMS T-Phase stations, and for Ascension Island. Tristan da Cunha is an island station, so calculations were performed in two directions, for hydroacoustic waves coming from the north and from the east. VIB is a coastal station, similar in many respects to the California/Point Sur geography, and the calculation for VIB was performed for normal incidence to the coastline. The Ascension Island calculation was performed for comparison with the Ascension Island experiments discussed in the following section. Calculations were performed for a source depth of 1000 meters except for one additional Tristan da Cunha calculation which was performed for a source depth of 2700 meters.

Figure 18 shows the bathymetric profiles used in each of the calculations. Also shown on the figures are lines representing slopes of 10, 20, and 30 degrees. Although the island slopes are quite steep compared to continental coastlines, they are still only a maximum of about 11 degrees in slope.

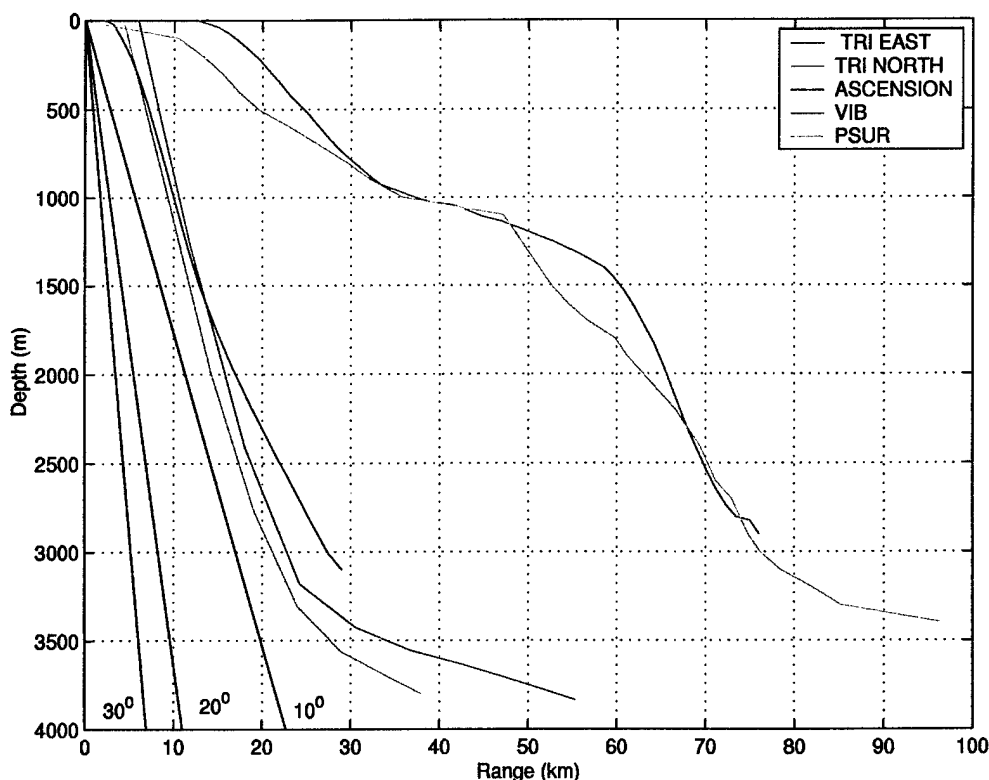


Figure 18. Bathymetry from the coastline to the starting point for each calculation. The slope offshore of Tristan da Cunha and Ascension Island is much steeper than the slope off the California coast, or near VIB. Note, however, that there is considerable vertical exaggeration in the plot, and that the steepest slope is only about 11 degrees.

Figure 19 shows a map of the bathymetry near the Tristan da Cunha IMS station, and the finite difference grid used to represent it. Note that the structure has a complex, three-dimensional shape that is not well represented by the two-dimensional geometry, and the calculation really should be performed in three-dimensions. Nevertheless, the two-dimensional calculation provides an approximate solution that shows the effect of the slope on the T-Phase conversion. Figure 20 shows a map of the bathymetry near the VIB T-Phase station. In this case, we expect the two-dimensional calculation to be a reasonably good representation of the actual geometry for waves at normal incidence.

Figure 21 shows the results of the calculations in the form of velocity spectra in the water, velocity spectra on land, and the ratio of spectra on land to spectra in the water, which corresponds to the T-Phase transfer function spectrum. Since we are comparing velocity to velocity instead of pressure, there is no material property conversion factor discussed in the previous section. The results are similar to the results of the previous calculations – there is an amplitude decrease due to conversion and the amplitude decrease is greater at higher frequency. These general characteristics are consistent, however there is a significant amount of variation in the spectral shape at higher frequencies. The reasons for these differences will require further research.

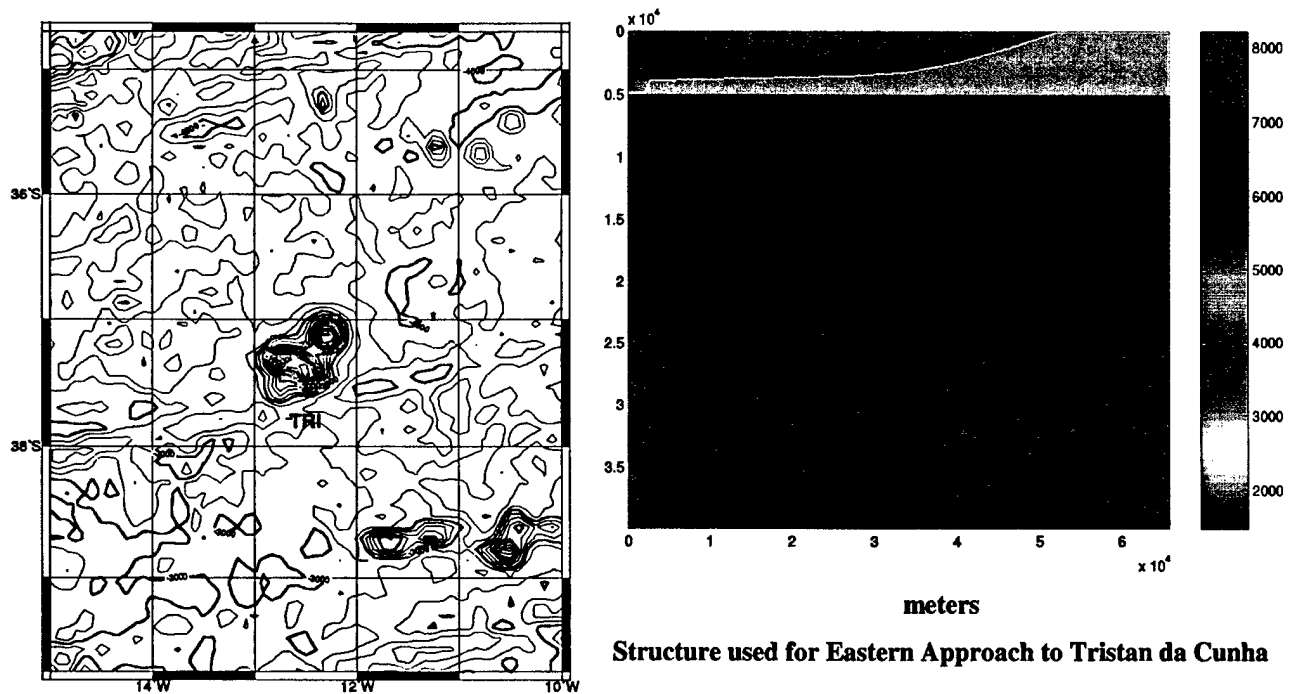


Figure 19. T-Phase conversion at the Tristan da Cunha IMS station is being modeled along profiles from the north and east. Modeling is being performed with 2D finite difference simulations. This type of structure may require 3D finite difference for accurate results.

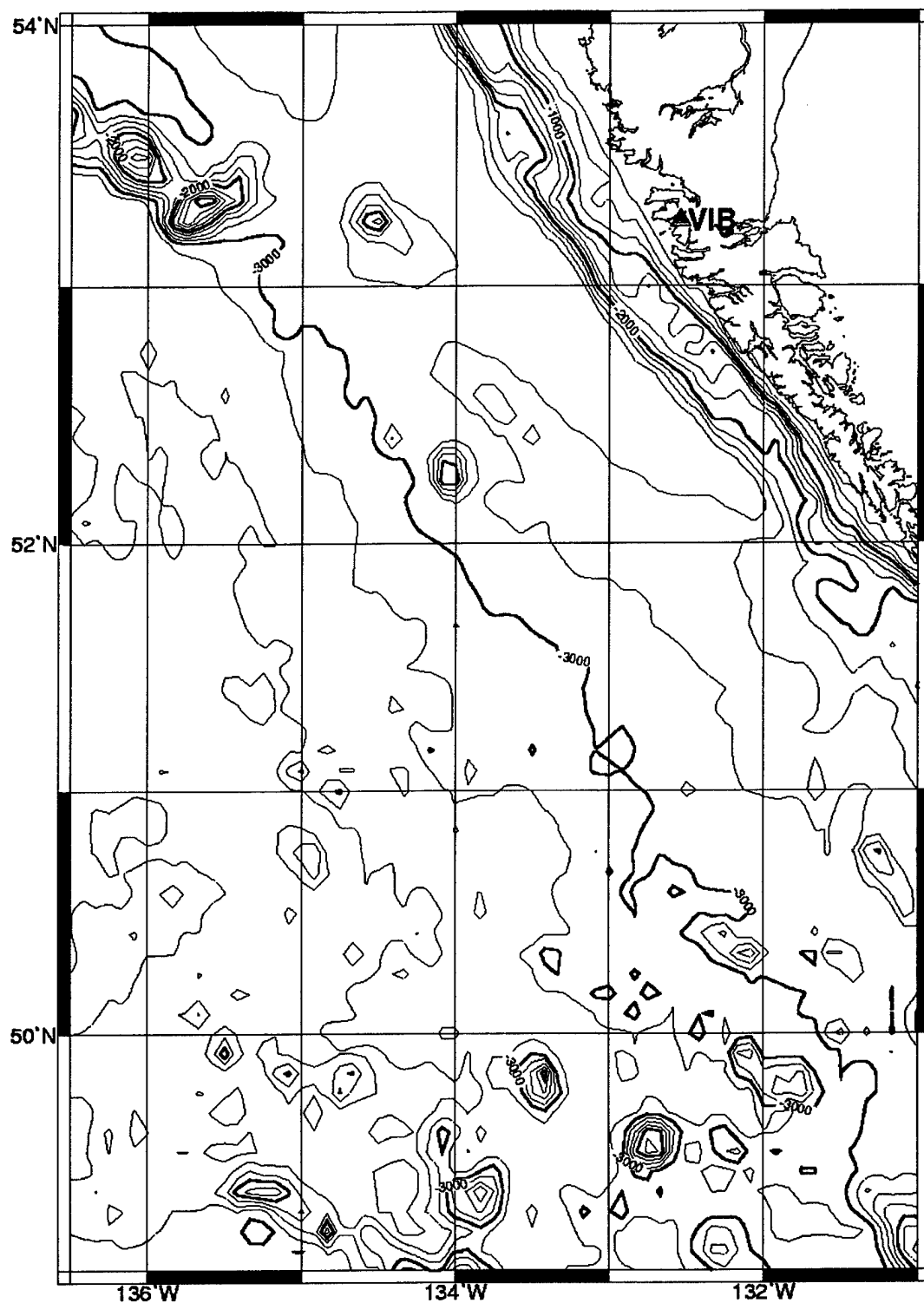


Figure 20. Bathymetry along the path to the IMS T-Phase station. VIB is similar to paths to the California stations.

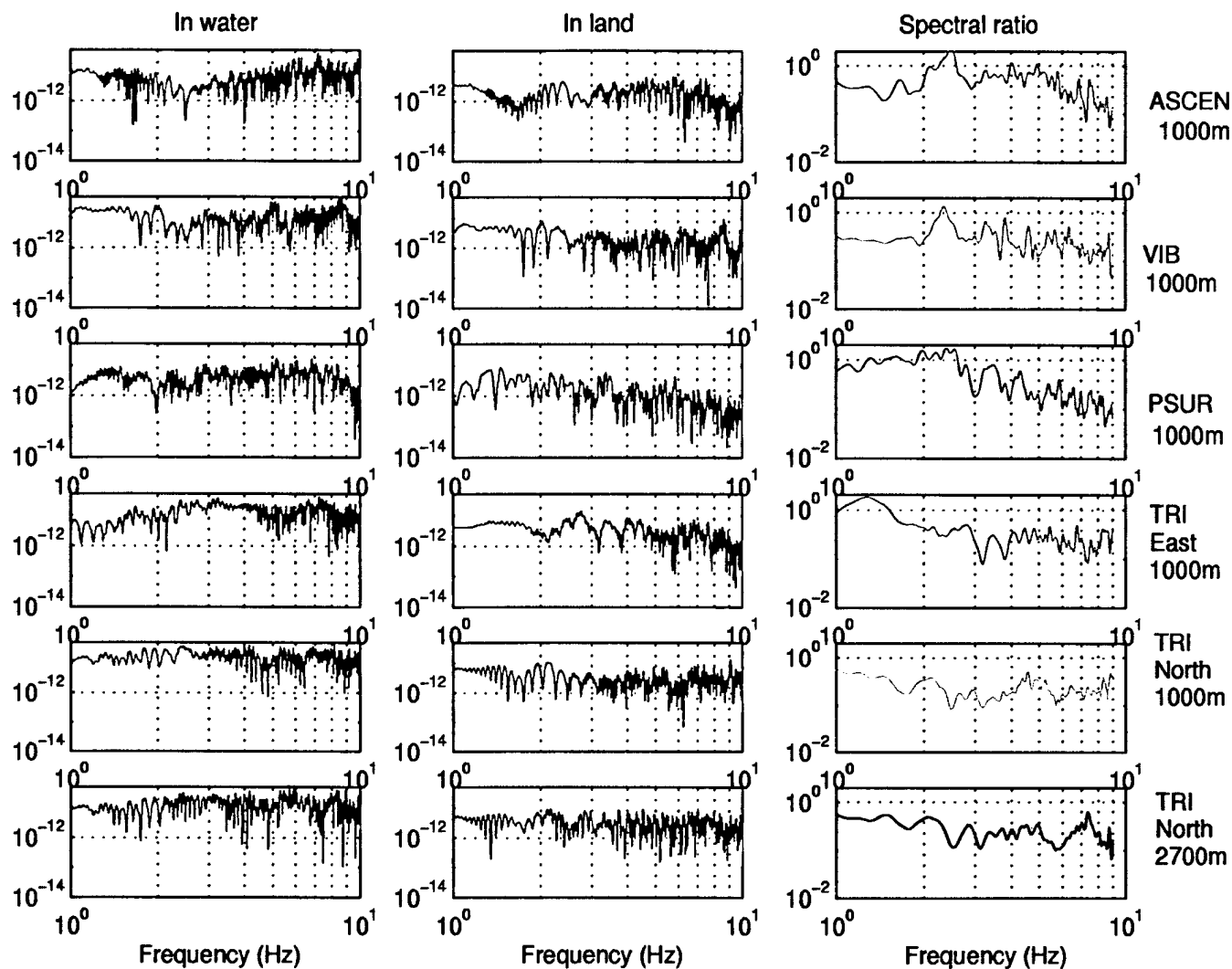


Figure 21. Calculated Spectra in Water and on Land. Left: Horizontal Velocity spectra in water at 350 m depth. Center: Vertical Velocity spectra on land one km from coast. Spectral ratio: ratio of spectrum on land to spectrum in water. The calculations from top to bottom are for Ascension island, VIB, Point Sur, Tristan da Cunha along a path from the East, Tristan da Cunha along a path from the North, and Tristan da Cunha along a path from the north with the source depth at 2700 m. In the first five calculations, the source depth was 1000 m.

Section 8

Ascension Island Experiment

The Ascension Island hydroacoustics experiment (Blackman, 1999a; Harben et al, 1999a) was conducted over a 4-day period in May, 1999, to determine the precise locations (Harben et al, 1999b) and calibrate the responses of (Harben et al, 2000) the set of three Missile Impact Location System (MILS) hydrophones to be used for one of the hydroacoustic stations in the International Monitoring System (IMS) for the Comprehensive Nuclear Test Ban Treaty. To permit calibration of the MILS hydrophones, two calibrated autonomous hydrophone data acquisition systems were deployed near the island by the Institute of Geophysics and Planetary Physics (IGPP), Scripps Institution of Oceanography (SIO). A total of 10 temporary, 3-component seismic stations also were installed on the island by the Lawrence Livermore National Laboratory (LLNL) to allow investigations of the water-to-land coupling characteristics. The layered volcanic structure of the island is very similar to the geology and surrounding bathymetry of several IMS T-phase stations. Therefore, this data set provides a great opportunity to study the T-phase transfer function characteristics in an environment relevant to the IMS. We derive an empirical transfer function of the coupling between the in-water acoustic field and the land seismic field. The resulting transfer function curves are compared to numerical simulations and to similarly-derived empirical transfer functions for the central California coast discussed earlier.

Data from the three MILS hydrophones, ASCH 23, 24, and 26, with a sampling rate of 120 samples/sec, were acquired from Keith McLaughlin of the Center for Monitoring Research. Phil Harben and Don Rock of LLNL kindly provided us with data from their 10 temporary seismic installations and their system response. In addition, Donna Blackman of IGPP/SIO gave us the data from the 2 calibrated hydrophone systems, called the Low-Cost Hardware for Earth Applications and Physical Oceanography (LCHEAPO). Both the LLNL seismic station data and the LCHEAPO data are sampled at 250 samples/sec. Donna and Jeff Babcock of IGPP/SIO also provided us with the information and programs required to calibrate the LCHEAPO data (<http://victory.ucsd.edu/obsh.html>). Finally, fine-scale measurements of bathymetry in certain regions about Ascension Island were sent to us by Tim Minshall of the Southampton Oceanography Center.

Ascension Island is the site of two permanent, 3-component seismometers buried at depths of 1 m and 100 m that are part of the Global Seismic Network (GSN) operated by the Incorporated Research Institutions for Seismology (IRIS). However, no useful data were recorded by these permanent stations during the experiment (Blackman, 1999b).

Ascension Island In-Water Receivers

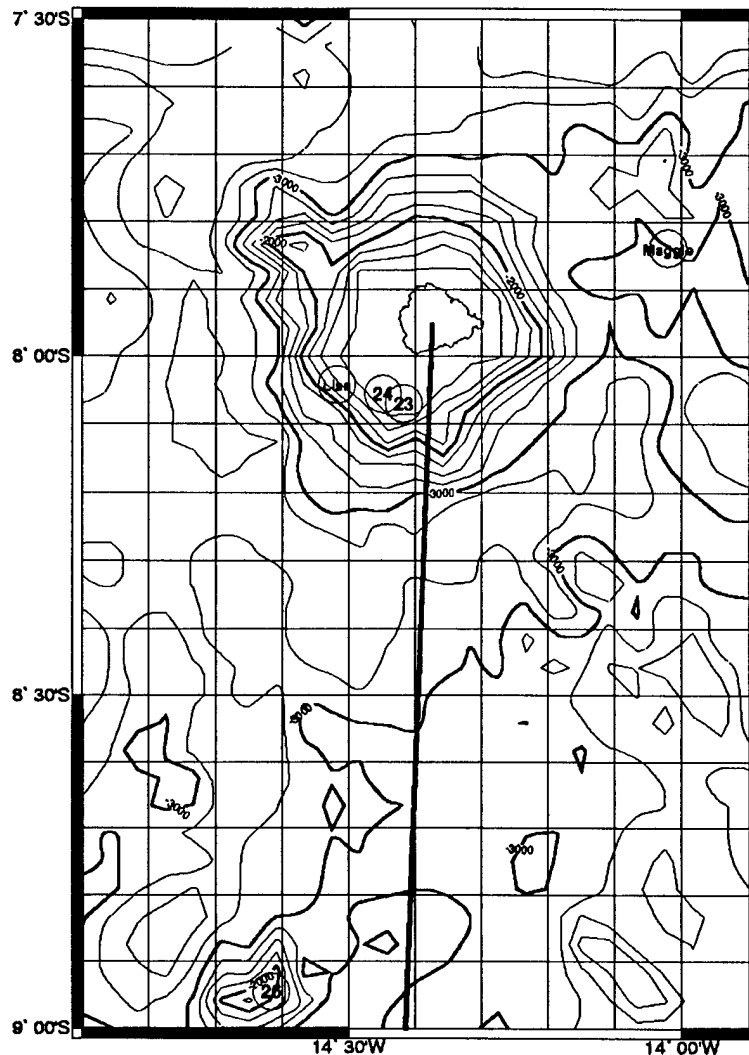


Figure 22. Map of Ascension Island along with the locations of the three MILS hydrophones ("23", "24", and "26") and the two LCHEAPO units ("Lisa" and "Maggie").

Figure 22 shows a map of Ascension Island along with the locations of the three MILS hydrophones ("23", "24", and "26") and the two LCHEAPO units ("Lisa" and "Maggie"). The two MILS hydrophones, ASCH 23 and 24, were located in approximately 800-m deep water, less than 10 km off the south coast of the island, and ASCH 26 is located an additional 100 km or so to the south in 1.66-km-deep water (Harben et al, 1999b). Lisa was deployed just to the west of ASCH 23 and 24 in nearly 1700-m-deep water and Maggie was deployed about 30 km to the northeast of the island in waters approaching 3000 m in depth. Whereas all three ASCH hydrophones are positioned on or near the ocean bottom (Harben et al, 1999b), the two LCHEAPO units were tethered up from the bottom to depths of 923 m (Lisa) and 1347 m (Maggie), near the sound channel axis (Blackman, 1999a). Figure 23 provides a finer-scale plot of the island itself showing the locations of the 10 LLNL seismic stations.

Ascension Island LLNL Stations

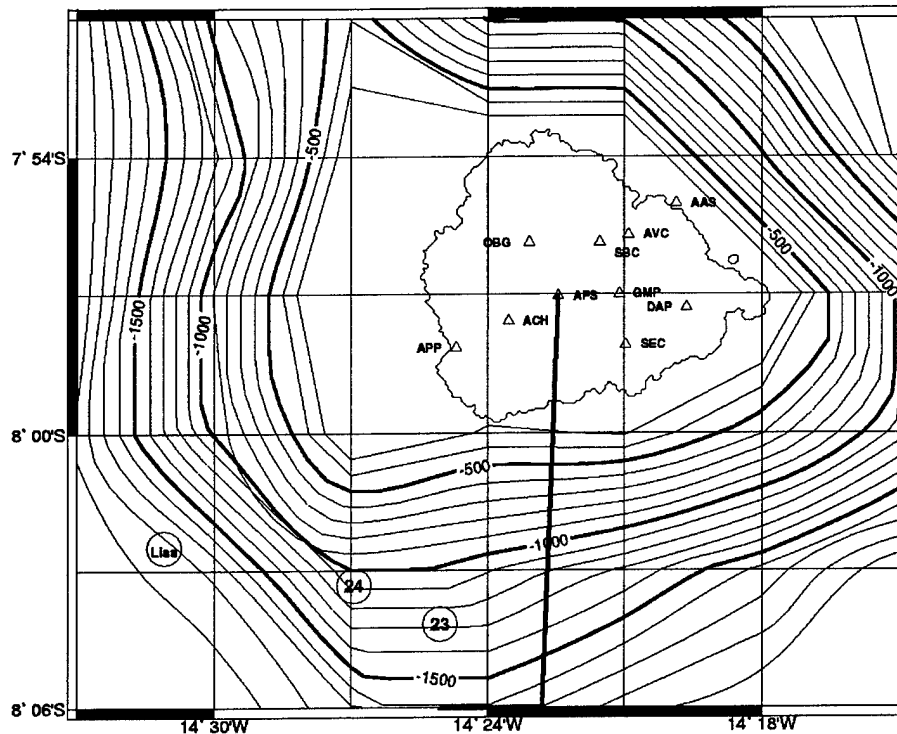


Figure 23. Map of the Ascension island itself showing the locations of the 10 LLNL seismic stations.

Continuous; 1-hour-duration, spectrograms of ASCH 23 and 24 data over the full duration of the experiment were created to provide a guide for more focused studies. In addition to the signals from the extensive air gun operations (Blackman, 1999a; Harben et al, 1999a), arrivals from several natural events that occurred during the experiment were identified (Blackman, 1999a, 1999b). These events are believed to be tectonic rather than volcanic in nature (Blackman, 1999b). Figure 24 shows the 60-min spectrogram from ASCH 23 containing one large, and a few smaller, natural events. The large event at 17:43 was identified in the Reviewed Events Bulletin (REB Event 20477344). This mb 4.2 event occurred at 1999 May 14, 17:10:08.7 GMT (JD 134) at 35.1078 S, 15.9247 W in the Tristan de Cunha region, a distance of approximately 2900 km to the south of Ascension Island. The time series and rms amplitude for this event (the "REB event") recorded by the three MILS hydrophones and Maggie are plotted in Figure 25. Unfortunately, Lisa was not recording data at this time.

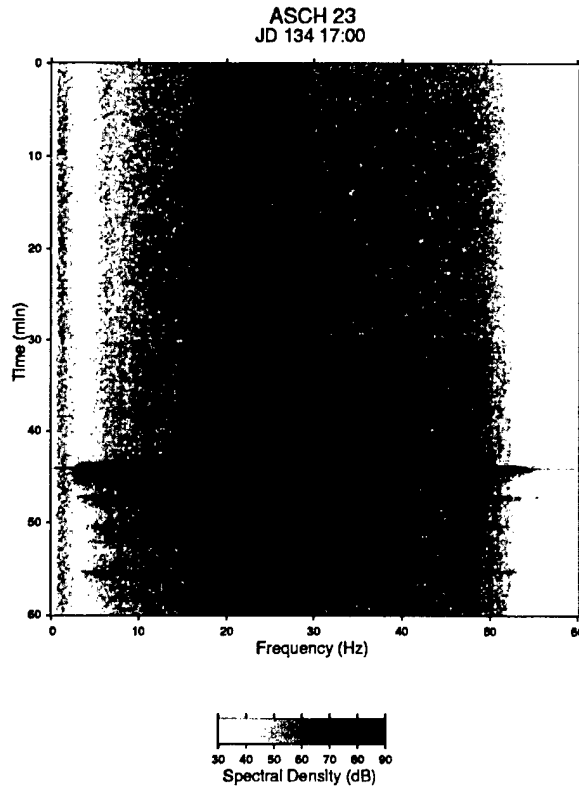


Figure 24. 60-min spectrogram from ASCH 23.

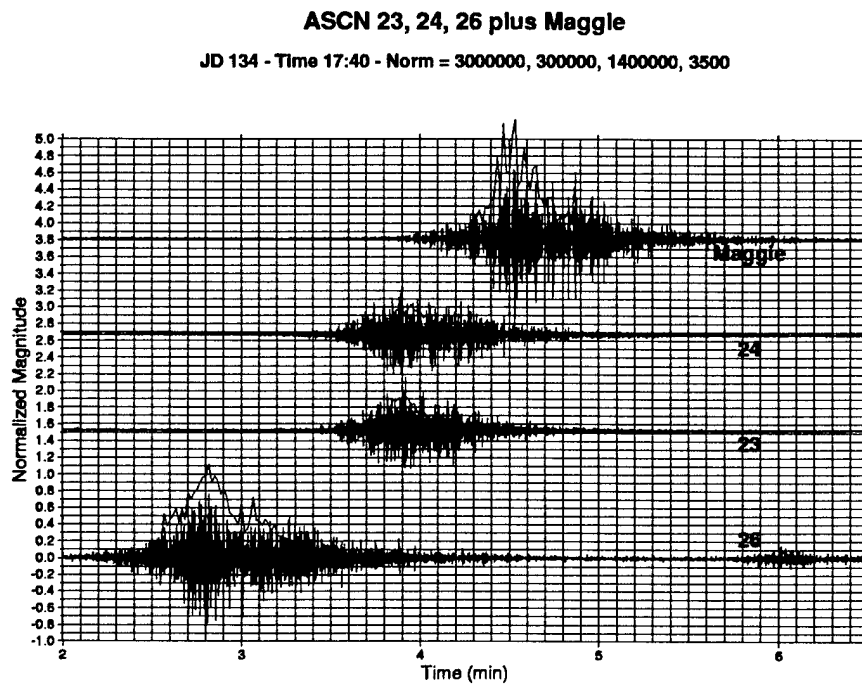


Figure 25. Time series and rms amplitude for the REB event recorded by the three MILS hydrophones and Maggie.

The land seismic station data were examined over the time periods corresponding to the occurrence of all natural events in the hydrophone data. Although associated arrivals on land could be seen for some of the events, only the mb 4.2 REB event was recorded at several stations with significant signal-to-noise ratio (SNR). Therefore, only this event was used to calculate empirical T-phase transfer functions, defined as the ratio of the on-land vertical component particle velocity spectrum to the in-water pressure spectrum. Plots of the time series for the vertical components for 8 of the 10 seismic stations are shown in Figure 26.

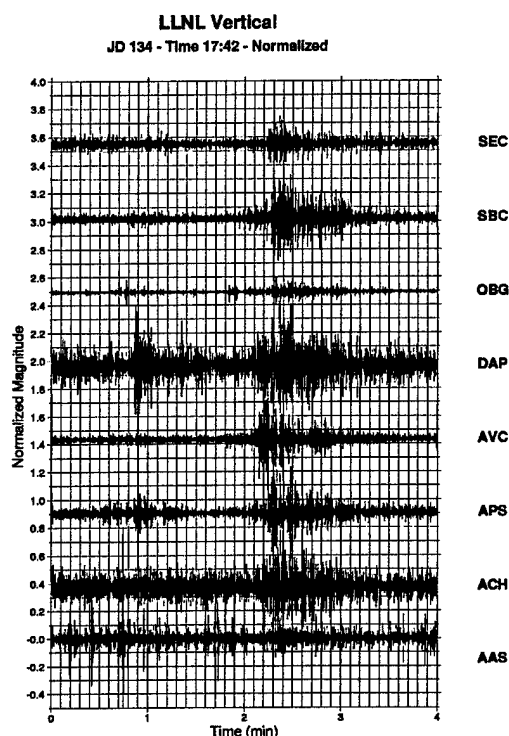


Figure 26. Time series for the vertical components for 8 of the 10 seismic stations.

These data were used to calculate the spectral levels of the arrivals and of the background noise to identify the frequency bands over which the SNR was greater than about 3 dB. The resulting frequency bands for each station determined the bands over which the empirical T-phase transfer functions were calculated. These bands are listed in Table 3.

Table 3. Frequency Bands having Significant SNR for REB Event.

| Land Station | Frequency Band (Hz) |
|--------------|---------------------|
| AVC | 2.5 - 18 |
| OBG | 2.5 - 16 |
| SEC | 2.5 - 14 |
| DAP | 2.5 - 12 |
| SBC | 2.5 - 11 |
| APS | 2.5 - 10 |
| APP | 2.5 - 10 |
| ACH | 2.5 - 6 |
| AAS | levels too low |
| GMP | no data |

As previously mentioned, the LCHEAPO instrument closest to Ascension Island, Lisa, was not operating during the REB event. Therefore, the only fully calibrated in-water system that recorded this event was Maggie, which was located some 30 km on the other side of the island in significantly deeper water. (Analysis of the air gun recordings by the MILS hydrophones by LLNL permitted only a frequency-independent calibration factor to be determined (Harben et al, 2000)). The approach used here was to estimate the calibrated spectrum that would have been recorded by Lisa based on data from nearby ASCH 23 and 24 and using a smaller natural event occurring later in the experiment. Arrivals from this "calibration event" were recorded at 23:45 GMT, JD 134, by all the in-water sensors shown in Figure 22. Therefore, an estimate of the calibrated Lisa spectrum for the REB event at 17:43 is:

$$\{ \text{Sp (Lisa at 17:43)} \} = \frac{\{ \text{Sp (ASCH 23,24 at 17:43)} \}}{\{ \text{Sp (ASCH 23,24 at 23:45)} \}} \times \{ \text{Sp (Lisa at 23:45)} \}$$

Spectral ratios for the two events recorded by ASCH hydrophones 23 and 24 (the ratio in the equation above) are shown in Figure 27. The consistency of this scaling factor estimated from these two sets of data provides a check on this approach.

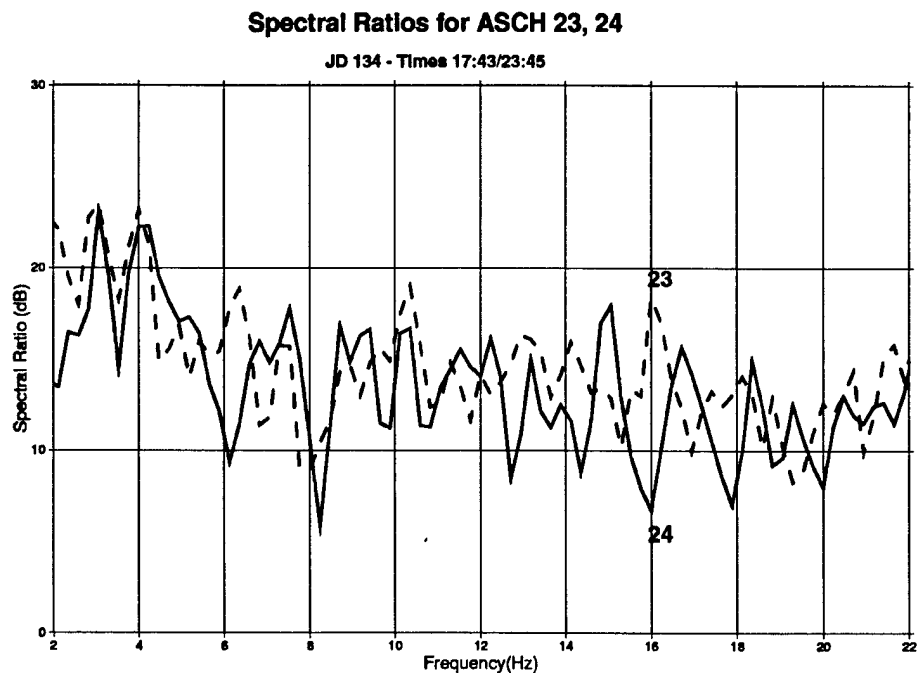


Figure 27. Spectral ratios for the two events recorded by ASCH hydrophones 23 and 24.

An alternate interpretation of the expression above can be obtained by rearranging terms on the right hand side. That is, the ratio of Lisa's calibrated spectrum to the Ascension hydrophone spectra for the 23:45 event provides a broadband calibration curve in amplitude for ASCH 23 and 24. Figure 28 shows plots of the ratio of the 23:45 event spectrum recorded by Lisa (in units of dB re 1 Lisa count) normalized by the uncalibrated spectra from ASCH 23 and 24 (in units of dB re 1 ASCH 23 count and dB re 1 ASCH 24 count, respectively). The offset of 14 dB between the two curves is equivalent to a factor of five, equal to the ratio of the counts/Pa values between ASCH 23 and 24 found in Harben et al, 2000. In the frequency band shown in Figure 28, the LCHEAPO response is approximately independent of frequency. Given a hydrophone sensitivity of -182.8 dB re 1 V/uPa (the loss of sensitivity of 2.5 dB per 3000 m depth has been taken into account), a software-preset voltage preamp gain value of 0 dB (equivalent to the minimum gain factor of 1), an automatic gain control value of 36.1 dB (equivalent to the maximum gain factor of 64), and an A/D conversion value of 83.3 dB re 1 cnt/V (representing a 16-bit A/D converter with a 4.5-volt input range), then the calibration factor for Lisa is -63.4 dB re 1 cnt/uPa = 56.6 dB re 1 cnt/Pa. Applying this calibration value to the spectral ratio level of the curves in Figure 28 results in a frequency dependent amplitude calibration curve for the two MILS hydrophones. The levels of these curves at 10 Hz, where the frequency-independent scaling factors in Harben et al are valid, are:

Table 4. Calibration Factors at 10 Hz for ASCH 23 and 24.

| Ascension Hydrophone | Cal Value at 10 Hz (dB re 1 cnt/Pa) | Cal Factor (cnts/Pa) | Harben et al (dB re 1 cnt/Pa) | Harben et al (cnts/Pa) |
|----------------------|-------------------------------------|----------------------|-------------------------------|------------------------|
| 23 | 99 dB | 8.9×10^4 | 84.6 dB | 1.7×10^4 |
| 24 | 113 dB | 44.7×10^4 | 99.0 dB | 8.8×10^4 |

The corresponding values found by Harben et al are listed in the last two columns. They differ by 14 dB, i.e., a factor of 5, from those found here. Interestingly, Harben et al, 2000 also provide both uncalibrated (their Figure 1) and calibrated (their Figure 3) airgun arrivals at Lisa. The peak-to-peak level of the first arrival in the uncalibrated plot is 13.1×10^6 counts and in the calibrated plot, 325 Pa, resulting in a scaling factor of 4.0×10^4 counts/Pa, or 92.1 dB re 1 cnt/Pa, a value which is 35.5 dB, or a factor of 60, greater. Therefore, it appears that the both the voltage gain preamp and the automatic gain control on Lisa were set at the maximum gain factor of 64 during the recording of these airgun events.

LISA/ASCH23 and LISA/ASCH24

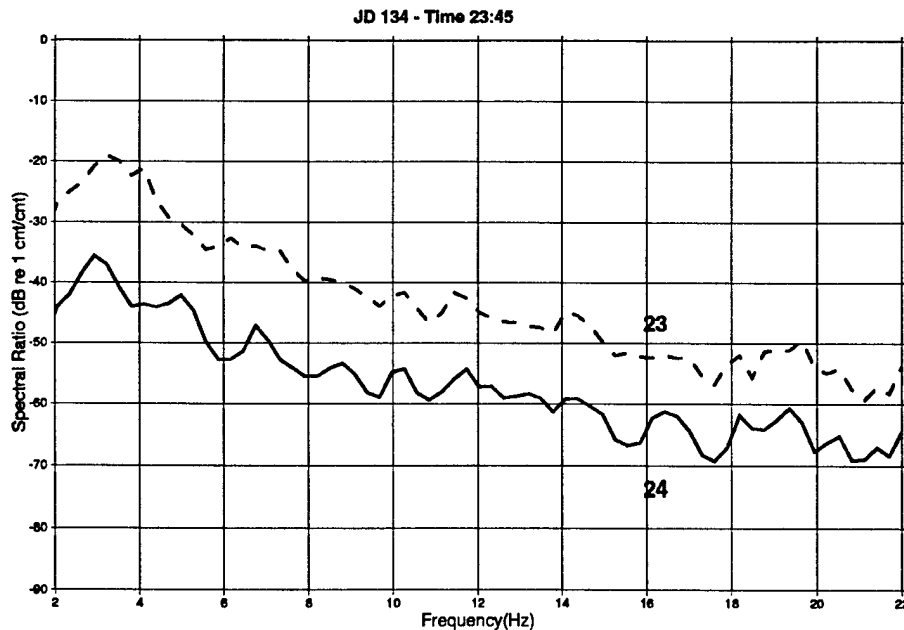


Figure 28. Ratio of the 23:45 event spectrum recorded by Lisa (in units of dB re 1 Lisa count) normalized by the uncalibrated spectra from ASCH 23 and 24.

Using the estimated calibrated pressure spectrum for the REB event at 17:43 to normalize the on-land vertical geophone spectra, the empirical T-phase transfer functions were calculated over the frequency bands specified in Table 1. The transfer functions for 6 of the 10 stations are plotted in Figure 29. Besides stations AAS and GMP, the results from OBG and APP are not presented since they deviated significantly from the other station results and are presumed contaminated by noise. The overall agreement for the six stations is striking. The curves asymptotically approach a value slightly less than -120 dB re 1 m/s/Pa as the frequency decreases. This value represents complete coupling of the in-water energy into land. That is, the constant of proportionality between the time-averaged, in-water, acoustic potential energy density (which is proportional to the acoustic pressure spectrum) and the time-averaged acoustic kinetic energy density (proportional to the sum of the individual component acoustic particle velocity spectra) is the square of the characteristic impedance of the ocean medium. For a nominal sound speed of 1.5 km/s and density 1000 kg/m³, this proportionality constant then is $2.25 \times 10^{12} \text{ (Pa/m/sec)}^2 = 123.5 \text{ dB re 1 Pa/m/sec}$. Therefore, if all the acoustic kinetic energy in the water column is converted into kinetic energy of motion on land, and the vertical component is representative of the overall land motion, then the value indicating optimal acoustic-to-seismic conversion in Figure 29 is -123.5 dB. This discussion does not take into account the effects of a free surface boundary condition at the earth-air interface, which can add 6 dB to the empirical transfer function.

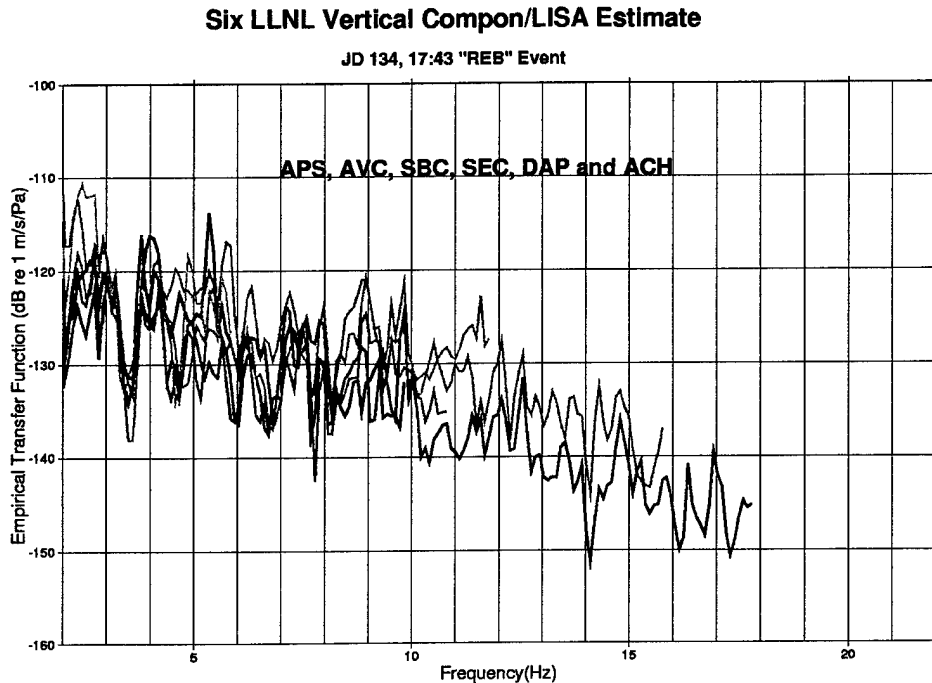


Figure 29. Transfer functions for 6 of the 10 stations.

Comparison of the results in Figure 29 with those for the coast of California, obtained from recordings at Pt. Sur and at the Berkeley Seismic Network of events in the Hawaiian Island region (Stevens et al, 1999), indicate that the empirical transfer function levels at the lowest frequencies are an order of magnitude lower in the latter case (less than -140 dB) than for Ascension. The transfer function levels for both environments decrease with increasing frequency, but those for the California coast decrease at a higher rate. Both the lower levels and the faster rolloff with frequency are associated with the coupling region being farther offshore and the bathymetry gradients being gentler in the California coastal environment.

As discussed in the previous section, numerical calculations of the T-phase transfer function for the Ascension Island experiment also have been conducted. The Kraken normal mode model (Porter, 1995) was used to model the ocean acoustic propagation along the first 2893 km of the great circle path from the event epicenter to a point just south of Ascension Island. The resulting in-water acoustic pressure and particle velocity fields for the lowest 10 normal modes then were provided as inputs to the TRES finite difference to model the coupling into the land seismic field. The ocean propagation path was divided into several consecutive, non-overlapping, range-independent sectors and an adiabatic normal mode approximation was used to model the range dependence of the medium. Bathymetry variations along the path, which determined the number and size of the range independent sectors, was obtained from the Sandwell 2-min-resolution data base (Sandwell et al, 1998). Water column sound speed profiles for each sector were extracted from the Scripps Institution of Oceanography NEMO web site (Scripps, 1998). The source depth was set at 1000 m (additional modeling results indicate that the transfer function is not very sensitive to source depth when the source is at great range). The calculations were done in 0.1 Hz increments from 1.0 to 9.0 Hz. Figure 21 in the previous section shows plots of the spectral

ratio of the on-land vertical particle velocity to the in-water horizontal particle velocity for several environments of relevance to the IMS. The third panel from the top in the left-hand column in Figure 21 is the calculation for the REB event coupling into Ascension Island. Note that overall levels at the lowest frequencies and the fact that the rolloff with frequency does not begin until 5-6 Hz are consistent with the data-derived results in Figure 29.

Section 9

Effect of Ocean Bottom Type on Long Range Hydroacoustic Propagation

Numerical studies were conducted to examine the sensitivity of the water column sound field to geoacoustic properties of the ocean bottom. The wavenumber integration program OASES (Schmidt, 1997) was used to perform the numerical modeling. In the five cases presented here, the source frequency and depth were fixed at 10 Hz and 1092 m, respectively. Also, the ocean medium was range independent with a 3000-m-deep water column having a characteristic mid-latitude deep water sound speed profile. The deep sound channel axis occurs at depths between 700 and 900 m. The received pressure field as a function of depth was evaluated at a range of 1000 km. Results are presented for the 5 different bottom types listed in Table 5.

Table 5. Bottom types used in this study.

| | Case 1 | Case 2 | Case 3 | Case 4 | Case 5 |
|------------------------|--------|--------|--------|--------|--------|
| Sediment thickness (m) | 1000 | 0 | 1000 | 1000 | 0 |
| Sediment C_p (km/s) | 2.1 | 0 | 2.1 | 2.1 | 0 |
| Sediment C_s (km/s) | 0.0 | 0 | 0.3 | 1.0 | 0 |
| Subbottom C_p (km/s) | 6.0 | 6.0 | 6.0 | 6.0 | 6.0 |
| Subbottom C_s (km/s) | 0.0 | 0.0 | 2.5 | 2.5 | 2.1 |

In all cases, the compressional and shear attenuations in the sediment layer were 0.0743 dB per wavelength, and in the subbottom 0.0209 dB per wavelength. The sediment and subbottom densities were 2.1 g/cc and 2.7 g/cc.

Plots of the normalized pressure field amplitude as a function of depth at 1000 km range are shown in Figs. 30 through 34 for the five cases. Changes in the pressure field with depth can result simply from a change in the relative phase relationship between modes. Therefore, to determine the effects of changes in bottom type on the relative mode amplitudes, the decomposition of the field into its normal mode components also is shown for each case. Comparison of the two pure fluid-bottom models, Case 1 and Case 2, shows that the effect of an attenuating fluid sediment layer is to decrease the overall received pressure levels by about 6 dB (a factor of 2 in amplitude). In addition, contributions from the higher order modes decrease so that the field displays somewhat less variability with depth. The introduction of shear into the sediment (cases 3 and 4) has a remarkable effect of stripping out the higher order modes, particularly as the shear speed approaches that of the sound speed in the water column. The resulting distribution of pressure with depth in these latter two cases provides a rough indication of source depth. However, once the bottom shear speed is increased to values greater than the water column sound speed (case 5), then contributions from higher order modes again become significant.

Case 1

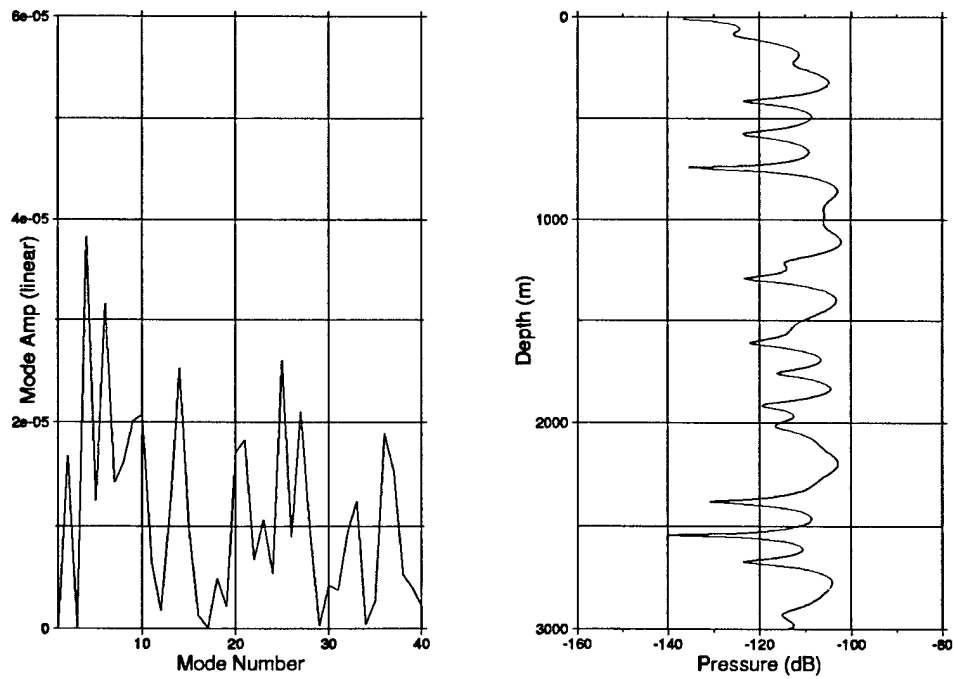


Figure 30. Normalized pressure field amplitude as a function of depth at 1000 km range Case 1.

Case 2

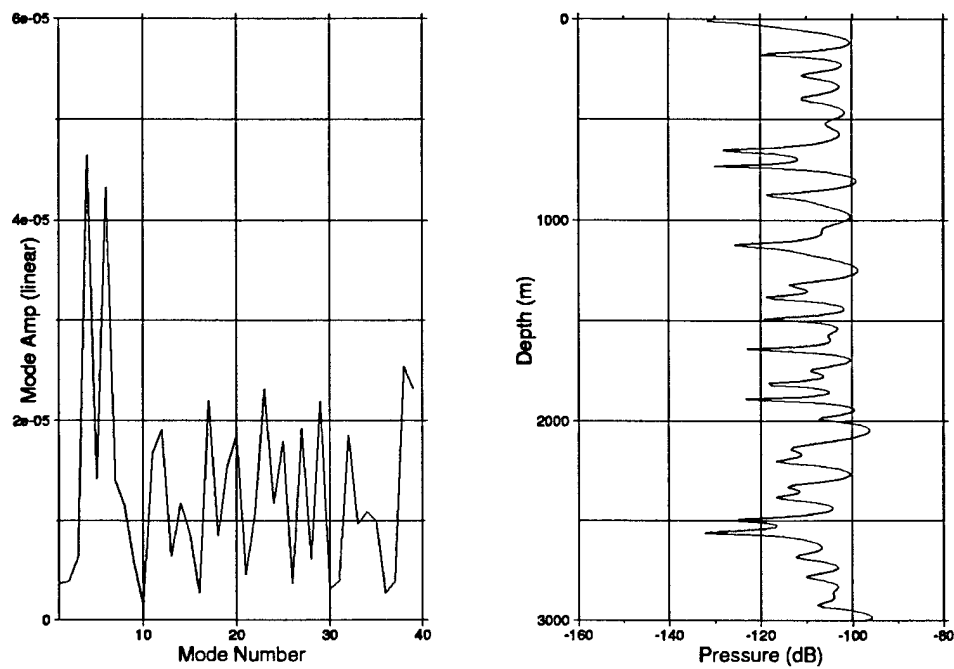


Figure 31. Normalized pressure field amplitude as a function of depth at 1000 km range Case 2.

Case 3

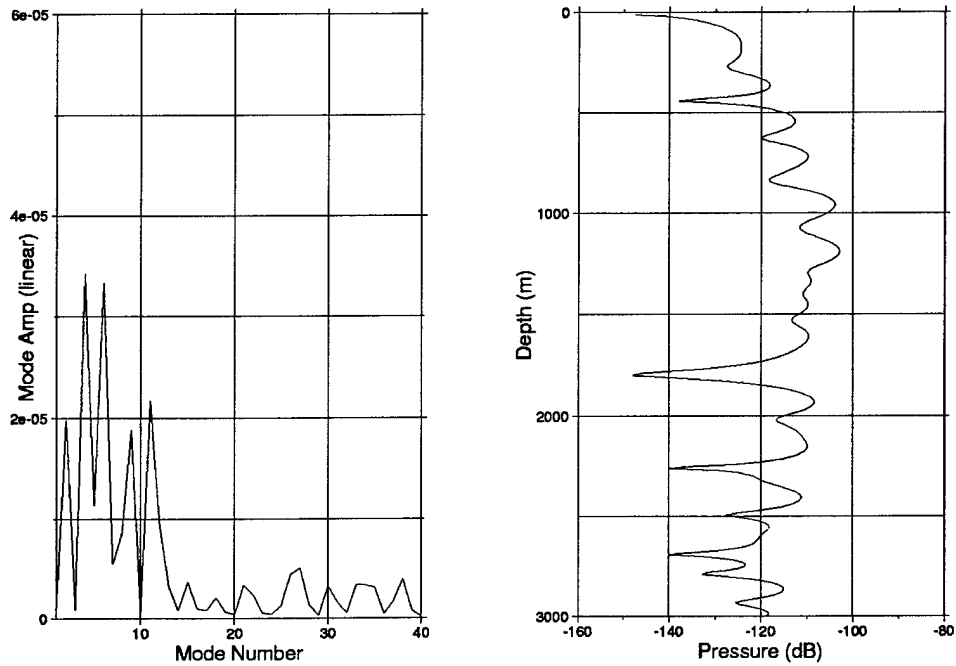


Figure 32. Normalized pressure field amplitude as a function of depth at 1000 km range Case 3.

Case 4

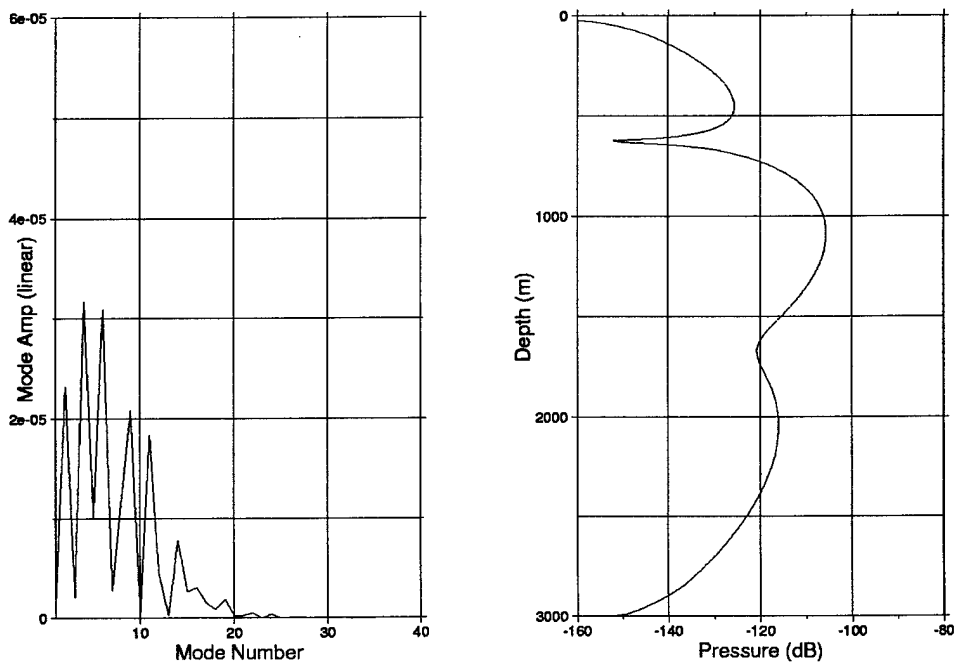


Figure 33. Normalized pressure field amplitude as a function of depth at 1000 km range Case 4.

Case 5

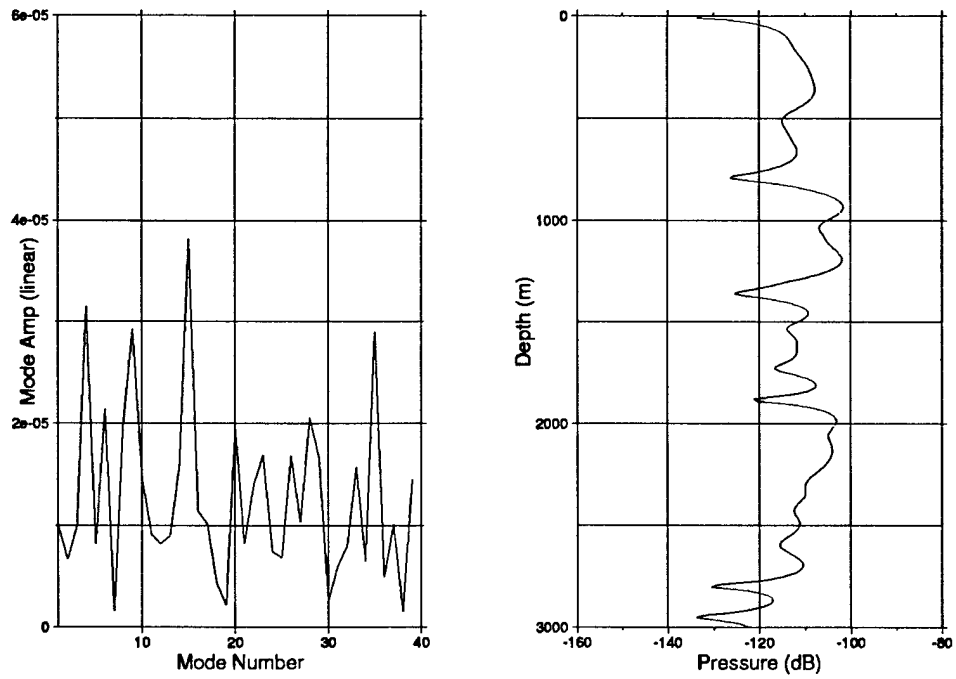


Figure 34. Normalized pressure field amplitude as a function of depth at 1000 km range Case 5.

Section 10

Conclusions and Recommendations

We have used observations of T-phases underwater and on land to directly measure the transmission of energy from ocean to land, and have performed numerical simulations of T-phase propagation from ocean to land to obtain a better understanding of this process. The observations show that there is a significant decline in spectral amplitude with frequency on land compared to observations in the ocean, but the decline is smaller with close proximity to the coast. The observations also show that T-phases propagate primarily as P-waves once they are far enough inland. The numerical simulations provide considerable insight into the phenomena that occur when hydroacoustic waves propagate onto land. The calculations reproduce the spectral degradation observed in Coastal California stations. Both the calculations and the observations show that T-phases observed near the coast are composed primarily of surface waves. Because the surface waves are generated over a more extended region than body waves, they may arrive at near coastal stations earlier than the body wave and obscure any body wave arrivals.

Continuing research is needed to evaluate the response of the IMS T-phase stations. The calculations and parameter studies performed to date provide considerable insight into the expected response at these stations. The calculations cover the range of slopes offshore of the IMS stations, and we have specifically modeled the propagation to stations VIB, Tristan da Cunha, and Ascension Island. Specific calculations of T-phase conversion should be performed for the remaining T-phase stations. Data should be gathered both underwater and on land at each of the IMS T-phase stations for comparison with the calculations and for a direct measurement of T-phase conversion. Three-dimensional calculations may be required to model the response of the island T-phase stations.

Section 11

References

Achenbach (1973), *Wave Propagation in Elastic Solids*, North-Holland Publishing Company, New York. (UNCLASSIFIED)

Blackman, D. K. (1999a), "Calibration of T-Phase recordings at Ascension Island: Signatures of natural and man-made sources," *Proc. 21st Annual Seismic Research Symposium: Technology for Monitoring the Comprehensive Nuclear Test Ban Treaty*, vol. II, pp. 1-7. (UNCLASSIFIED)

Blackman, D. K. (1999b), Private communication. (UNCLASSIFIED)

Cansi, Y. and N. Bethoux (1985), "T waves with long inland paths: synthetic seismograms," *J. Geophys. Res.*, V. 90, pp. 5459-5465. (UNCLASSIFIED)

Caplan-Auerbach, J., F. K. Duennebie, P. Okubo, and L. Kong (1999), "Seismicity and velocity structure of the Loihi Seamount from the 1996 earthquake swarm," in preparation. (UNCLASSIFIED)

Cook, R. W. and J. L. Stevens (1998), "TP Phase Observations at the pIDC," *Transactions of the American Geophysical Union*, v. 79, P. F558, November. (UNCLASSIFIED)

D'Spain, G. L., L. P. Berger, W. A. Kuperman, J. L. Stevens, and G. E. Baker (1999), "Normal mode composition of earthquake T-phases," submitted to *Pure and Appl. Geophys.* (UNCLASSIFIED)

Eneva, M., J. L. Stevens, J. R. Murphy, and B. D. Khristoforov (2000), "Effect of charge depth in Russian hydroacoustic data from nuclear and HE explosions," *Proceedings of the 22nd Annual DOD/DOE Seismic Research Symposium*, 12-15 September, 2000. (UNCLASSIFIED)

Eneva, M., J. L. Stevens, B. D. Khristoforov, J. R. Murphy, and V. V. Adushkin (2001), "Analysis of Russian Hydroacoustic Data for CTBT Verification", *Pure and Applied Geophysics*, in press. (UNCLASSIFIED)

Eneva, M., J. L. Stevens, J. Murphy, B. D. Khristoforov and V. V. Adushkin (1999), "Analysis of Russian Hydroacoustic Data for CTBT Verification", *Proceedings of the 21st Seismic Research Symposium on Monitoring a Comprehensive Test Ban Treaty*, 21-24 September, 1999. (UNCLASSIFIED)

Harben, P. E., Rock, D., and Rodgers, A. J. (1999a), "The Ascension Island hydroacoustic experiment: purpose, data set features, and plans for future analysis," *Proc. 21st Annual Seismic Research Symposium: Technol. for Monitoring the Comprehensive Nuclear Test Ban Treaty*, vol. II, pp. 36-46. (Unclassified)

Harben, P. E., Hollfelder, J. R., and Rodgers, A. J. (1999b), "Experimentally determined coordinates for three MILS hydrophones near Ascension Island," LLNL Tech. Rept. UCRL-ID-136507, Lawrence Livermore Nat'l Lab, 9 pgs. (UNCLASSIFIED)

Harben, P. E., Blackman, D. K., Rodgers, A. J., Turpin, C., and Hollfelder, J. R. (2000), "Calibration factors for three MILS hydrophones near Ascension Island," LLNL Tech. Rept. UCRL-ID-138036, Lawrence Livermore Nat'l Lab, 18 pgs. (UNCLASSIFIED)

McLaughlin, K. L. and S. M. Day (1994), "3D Elastic Finite-Difference Seismic-Wave Simulations, Computers in Physics," 8, #6, pp 656-663. (UNCLASSIFIED)

Mooney, W. D., G. Laske and T. Guy Masters (1998), "Crust 5.1: A global crustal model at 5°x5°," Journal of Geophysical Research, 103, 727-747. (UNCLASSIFIED)

NOAA (1998), "5-Min Global Digital Terrain Models," Web site of the National Geophysical Data Center, <http://www.ngdc.noaa.gov/seg/fliers/se-1104.html>. (UNCLASSIFIED)

Oliver, J. and M. Ewing (1958), "Short-Period Oceanic Surface Waves of the Rayleigh and First Shear Modes," Transactions of the American Geophysical Union, 30, 482-485. (UNCLASSIFIED)

Piserchia, P. F., J. Virieux, D. Rodrigues, S. Gaffet and J. Talandier (1998), "Hybrid numerical modelling of T-wave propagation: application to the Midplate experiment," Geophys. J. Int., V. 133, pp 789-800. (UNCLASSIFIED)

Porter, M. B. (1995), "The Kraken normal mode program", user's manual, SACLANT Undersea Research Centre, La Spezia, Italy. (UNCLASSIFIED)

Rodgers, A. J. and Harben, P. E., (1999), "Modeling the conversion of hydroacoustic to seismic energy at islands and continental margins: preliminary analysis of Ascension Island data," Proc. 21st Annual Seismic Research Symposium: Technol. for Monitoring the Comprehensive Nuclear Test Ban Treaty, vol. II, pp. 66-69. (UNCLASSIFIED)

Sandwell, D. T., Smith, W. H. F., Smith, S. M., and Small, C. (1998), "Measured and estimated seafloor topography," web site, http://topex.ucsd.edu/marine_topo/mar_topo.html. (Unclassified)

Schmidt, H. (1997), "OASES: Version 2.1, user guide and reference manual," Tech. Rept., Massachusetts Institute of Technology. (Unclassified)

Scripps Institution of Oceanography (1998), NEMO Oceanographic Data Server web site, National Oceanographic Data Center's Station Data File, <http://nemo.ucsd.edu/hs.html>. (Unclassified)

Stevens, Jeffery L., G. Eli Baker, Ron W. Cook, Gerald D'Spain, Lewis P. Berger, and Steven M. Day (2001), "Empirical and Numerical Modeling of T-Phase Propagation from Ocean to Land", Pure and Applied Geophysics, to appear Mar, 2001. (UNCLASSIFIED)

Stevens, Jeffry L., G. Eli Baker, Heming Xu, Gerald D'Spain and Lewis P. Berger (2000), "Finite Difference Modeling of T-Phase Propagation from Ocean to Land," Proceedings of the 22nd Annual DOD/DOE Seismic Research Symposium, 12-15 September, 2000. (UNCLASSIFIED)

Stevens, Jeffry L., G. Eli Baker, Ron W. Cook, Gerald D'Spain, Lewis P. Berger, and Steven M. Day (1999), "Empirical and Numerical Modeling of T-Phase Propagation From Ocean to Land", Proceedings of the 21st Seismic Research Symposium on Monitoring a Comprehensive Test Ban Treaty, 21-24 September, 1999. (UNCLASSIFIED)

Stevens, J. L., G. E. Baker, J. R. Murphy, R. W. Cook, G. D'Spain, L. P. Berger, and B. D. Khristoforov (1998), "T-Phase Excitation and Transfer Function Research," Proceedings of the 20th Seismic Research Symposium on Monitoring a Comprehensive Test Ban Treaty, 21-23 September. (UNCLASSIFIED)

Stevens, J. L. and K. L. McLaughlin (1997), "Improved Methods for Regionalized Surface Wave Analysis," Maxwell Technologies Final Report submitted to Phillips Laboratory, MFD-TR-97-15887, September. (UNCLASSIFIED)

Talandier, J. and E. A. Okal (1998), "On the mechanism of conversion of seismic waves to and from T waves in the vicinity of island shores," Bull. Seism. Soc. Am., V.88, pp. 621-632. (UNCLASSIFIED)

**DISTRIBUTION LIST
DTRA-TR-01-15**

DEPARTMENT OF DEFENSE

DIRECTOR
DEFENSE INTELLIGENCE AGENCY
BUILDING 6000, BOLLING AFB
WASHINGTON, DC 20340 5100
ATTN: DTIB

DIRECTOR
DEFENSE RESEARCH & ENGINEERING
WASHINGTON, DC 20301 3110
ATTN: DDR&E, ROOM 3E808

DEFENSE TECHNICAL INFORMATION CENTER
8725 JOHN J KINGMAN ROAD SUITE 0944
FORT BELVOIR, VA 22060 6218
2 CYS ATTN: DTIC/OCP

DEFENSE THREAT REDUCTION AGENCY
8725 JOHN J KINGMAN RD MS 6201
FORT BELVOIR, VA 22060 6201
ATTN: TDND, DR A DAINTY
ATTN: TDND, LTC T. CARTLEDGE

OFFICE OF THE SECRETARY OF DEFENSE
NUCLEAR TREATY PROGRAMS OFFICE
1515 WILSON BOULEVARD, SUITE 720
ARLINGTON, VA 22209
ATTN: P. WAKEFIELD
ATTN: DR. S. MANGINO

DEPARTMENT OF THE ARMY

US ARMY SMDC
ATTN SMDC- TC- YD
P.O. BOX 1500
HUNTSVILLE, AL 35807 3801
ATTN: B. ANDRE

DEPARTMENT OF THE AIR FORCE

AIR FORCE RESEARCH LABORATORY
29 RANDOLPH RD
HANSCOM AFB, MA 01731
ATTN: RESEARCH LIBRARY
ATTN: VSBL, R. RAISTRICK

USAF AT USGS
2201 SUNRISE VALLEY DRIVE MS 951
RESTON, VA 20192
ATTN: R. BLANDFORD
ATTN: R. JIH

AIR FORCE TECHNICAL APPLICATIONS CTR
1030 S HIGHWAY AIA
PATRICK AFB, FL 32925 3002
ATTN: CA, STINFO
ATTN: TTR, D. CLAUTER
ATTN: CTI, DR. B. KEMERAIT
ATTN: TT, DR. D. RUSSELL
ATTN: TTR, F. SCHULT
ATTN: TTR, G. ROTHE
ATTN: TTR, V. HSU
ATTN: DR. B. NGUYEN
ATTN: DR. E. SMART
ATTN: DR. G. WAGNER
ATTN: DR. M. WOODS
ATTN: DR. N. YACOUN

DEPARTMENT OF THE NAVY

NAVAL RESEARCH LABORATORY
4555 OVERLOOK AVE SW CODE 7643
WASHINGTON, DC 20375 0001
ATTN: DR, D. DROB

DEPARTMENT OF ENERGY

NATIONAL NUCLEAR SECURITY
ADMINISTRATION
1000 INDEPENDENCE AVE SW
WASHINGTON, DC 20585 0420
ATTN: L. CASEY
ATTN: M. DENNY
ATTN: G. KIERNAN

UNIVERSITY OF CALIFORNIA
LAWRENCE LIVERMORE NATIONAL LAB
P.O. BOX 808
LIVERMORE, CA 94551 9900
ATTN: MS L205, DR.D. HARRIS
ATTN: MS L208, TECHNICAL STAFF
ATTN: MS 205, TECHNICAL STAFF

**DISTRIBUTION LIST
DTRA-TR-01-15**

LOS ALAMOS NATIONAL LABORATORY
P.O. BOX 1663
LOS ALAMOS, NM 87545

ATTN: MS C335, DR. S. R. TAYLOR
ATTN: MS D460, FRANCESCA CHAVEZ
ATTN: MS D335, TECHNICAL STAFF
ATTN: MS D460, TECHNICAL STAFF
ATTN: MS F665, TECHNICAL STAFF
ATTN: MS D408, TECHNICAL STAFF
ATTN: MS J577, TECHNICAL STAFF
ATTN: MS D443, TECHNICAL STAFF

PACIFIC NORTHWEST NATIONAL LABORATORY
P.O. BOX 999
1 BATTELLE BOULEVARD
RICHLAND, WA 99352

ATTN: MS P8-20, T. HEIMBIGNER
ATTN: MS K8-29, DR. N. WOGMAN

SANDIA NATIONAL LABORATORIES
MAIL SERVICES
P.O. BOX 5800
ALBUQUERQUE, NM 87185 1363
ATTN: MS 1138, TECHNICAL STAFF
DEPARTMENT 6533

OTHER GOVERNMENT

DEPARTMENT OF STATE
2201 C STREET NW
WASHINGTON, DC 20520
ATTN: R. MORROW, ROOM 5741

NATIONAL ARCHIVES & RECORDS
ADMINISTRATION
8601 ADELPHI ROAD, ROOM 3360
COLLEGE PARK, MD 20740 6001
2 CYS ATTN: USER SERVICE BRANCH

US GEOLOGICAL SURVEY
ADVANCED SYSTEMS CENTER
MS 562
RESTON, VA 20192
ATTN: W. LEITH

US GEOLOGICAL SURVEY
345 MIDDLEFIELD RD MS 977
MENLO PARK, CA 94025
ATTN: S. DETWEILER
ATTN: DR. W. MOONEY

**DIRECTORY OF OTHER LIBRARIES AND
UNIVERSITIES**

BOSTON COLLEGE
INSTITUTE FOR SPACE RESEARCH
140 COMMONWEALTH AVENUE
CHESTNUT HILL, MA 02167
ATTN: DR. D. HARKRIDER
ATTN: B. SULLIVAN

BROWN UNIVERSITY
DEPARTMENT OF GEOLOGICAL SCIENCES
75 WATERMAN STREET
PROVIDENCE, RI 02912 1846
ATTN: PROF D. FORSYTH

CALIFORNIA INSTITUTE OF TECHNOLOGY
DIVISION OF GEOLOGY & PLANETARY SCIENCES
PASADENA, CA 91125
ATTN: PROF DONALD V HELMBERGER
ATTN: PROF THOMAS AHRENS

UNIVERSITY OF CALIFORNIA BERKELEY
281 MCCONE HALL
BERKELEY, CA 94720 2599
ATTN: PROF. B. ROMANOWICZ
ATTN: DR. D. DREGER

UNIVERSITY OF CALIFORNIA DAVIS
ONE SHIELDS AVENUE
DAVIS, CA 95616
ATTN: DIV STATISTICS, R.H.
SHUMWAY

UNIVERSITY OF CALIFORNIA SAN DIEGO
9500 GILLMAN DRIVE
LA JOLLA, CA 92093 0225
ATTN: DR.L. DEGROOT - HEDLIN
ATTN: DR. M. HEDLIN
ATTN: PROF F. VERNON
ATTN: PROF J BERGER
ATTN: PROF J. ORCUTT
ATTN: DR. G. D'SPAIN

UNIVERSITY OF CALIFORNIA SANTA CRUZ
INSTITUTE OF TECTONICS
1156 HIGH STREET
SANTA CRUZ, CA 95064
ATTN: DR. R. S. WU
ATTN: PROF T. LAY

DISTRIBUTION LIST
DTRA-TR-01-15

UNIVERSITY OF COLORADO BOULDER
DEPT OF PHYSICS
P.O. BOX 390
BOULDER, CO 80309 0390
ATTN: DR. A. LEVSHIN
ATTN: DR. R. ENGDAHL
ATTN: M. RITZWOLLER
ATTN: PROF C. ARCHAMBEAU

COLUMBIA UNIVERSITY
LAMONT DOHERTY EARTH OBSERVATORY
P.O. BOX 1000
61 ROUTE 9W
PALISADES, NY 10964
ATTN: DR. J. XIE
ATTN: DR. W. Y. KIM
ATTN: PROF P.G. RICHARDS
ATT N: DR. M. TOLSTORY

UNIVERSITY OF CONNECTICUT
DEPARTMENT OF GEOLOGY & GEOPHYSICS
BEACH HALL, UNIT 2045
STOORS, CT 06269 2045
ATTN: PROF V.F. CORMIER, U-45,
ROOM 207

CORNELL UNIVERSITY
DEPARTMENT OF GEOLOGICAL SCIENCES
3126 SNEE HALL
ITHACA, NY 14853
ATTN: PROF M.A. BARAZANGI

HARVARD UNIVERSITY
HOFFMAN LABORATORY
20 OXFORD STREET
CAMBRIDGE, MA 02138
ATTN: PROF A. DZIEWONSKI
ATTN: PROF G. EKSTROM

INDIANA UNIVERSITY
DEPARTMENT OF GEOLOGICAL SCIENCES
1005 10TH STREET
BLOOMINGTON, IN 47405
ATTN: PROF G. PAVLIS

IRIS
1200 NEW YORK AVENUE SUITE 800
WASHINGTON, DC 20005
ATTN: DR.D. SIMPSON
ATTN: DR.G.E. VAN DER VINK

IRIS
1408 NE 45TH ST #201
SEATTLE, WA 98105
ATTN: DR. T. AHERN

MASSACHUSETTS INSTITUTE OF TECHNOLOGY
EARTH RESOURCES LABORATORY
42 CARLETON STREET
CAMBRIDGE, MA 02142
ATTN: DR. W. RODI
ATTN: PROF M. N. TOKOZ

MICHIGAN STATE UNIVERSITY LIBRARY
450 ADMINISTRATION BUILDING
EAST LANSING, MI 48824
ATTN: K. FUJITA

NEW MEXICO STATE UNIVERSITY
DEPARTMENT OF PHYSICS
P.O. BOX 30001, MSC 3D
LAS CRUCES, NM 88003
ATTN: PROF J. NI
ATTN: PROF T. HEARN

NORTHWESTERN UNIVERSITY
DEPARTMENT OF GEOLOGICAL SCIENCES
1847 SHERIDAN RD
EVANSTON, IL 60208
ATTN: PROF E. OKAL

PENNSYLVANIA STATE UNIVERSITY
GEOSCIENCES DEPARTMENT
403 DEIKE BUILDING
UNIVERSITY PARK, PA 16802
ATTN: PROF C. AMMON
ATTN: PROF S. ALEXANDER
ATTN: DR. A. NYBLADE

**DISTRIBUTION LIST
DTRA-TR-01-15**

SAN DIEGO STATE UNIVERSITY
DEPARTMENT OF GEOLOGICAL SCIENCES
MC-1020
5500 CAMPANILE DRIVE
SAN DIEGO, CA 92182-1020
ATTN: PROF S.M. DAY

SOUTHERN METHODIST UNIVERSITY
DEPARTMENT OF GEOLOGICAL SCIENCES
P.O. BOX 750395
DALLAS, TX 75275
ATTN: B. STUMP
ATTN: E. HERRIN
ATTN: H.L. GRAY
ATTN: P. GOLDEN

UNIVERSITY OF HAWAII-MANOA
P.O. BOX 1599
KAILUA-KONA, HI 96745 1599
ATTN: DR. M. A. GARCES

UNIVERSITY OF MISSISSIPPI
1 COLISEUM DRIVE
UNIVERSITY, MS 38677
ATTN: PROF H. BASS

UNIVERSITY OF SOUTHERN CALIFORNIA
520 SEAVER SCIENCE CENTER
UNIVERSITY PARK
LOS ANGELES, CA 90089 0483
ATTN: PROF C.G. SAMMIS
ATTN: PROF T. JORDAN

WASHINGTON UNIVERSITY
DEPARTMENT OF EARTH PLANET SCIENCE
ONE BROOKINGS DRIVE
SAINT LOUIS, MO 63130 4899
ATTN: DR. G. SMITH

UNIVERSITY OF WISCONSIN MADISON
1215 W DAYTON ST
MADISON, WI 53706 1600
ATTN: DR. C. THURBER

ST LOUIS UNIVERSITY
P.O. BOX 8148
PIERRE LACLEDE STATION
ST LOUIS, MO 63156 8148
ATTN: PROF B.J. MITCHELL
ATTN: PROF R. HERRMAN

UNIVERSITY OF MEMPHIS
3890 CENTRAL AVE
MEMPHIS, TN 38152
ATTN: DR. J. PUJOL
ATTN: DR. C. LANGSTON

UNIVERSITY OF TEXAS AUSTIN
P.O. BOX 7726
AUSTIN, TX 78712
ATTN: DR. J. PULLIAM
ATTN: DR. M. SEN

UNIVERSITY OF TEXAS EL PASO
DEPT OF GEOLOGICAL SCIENCES
MAIL CODE: 00555
EL PASO, TX 79968
ATTN: PROF G. KELLER
ATTN: DR. D. DOSER
ATTN: DR. A. VELASCO

FOREIGN

AUSTRALIAN GEOLOGICAL SURVEY
ORGANIZATION
CORNER OF JERRAGOMRRRA &
NINDMARSH DRIVE
CANBERRA, ACT 2609 AUSTRALIA
ATTN: D. JEPSON

GEOPHYSICAL INSTITUTE OF ISRAEL
POB 182
LOD, 71100 ISRAEL
ATTN: DR. Y. GITTERMAN
ATTN: DR. A. SHAPIRA

GEOLOGICAL SURVEY OF CANADA
7 OBSERVATORY CRESCENT
OTTAWA K1A 0Y3 ONT
CANADA
ATTN: C. WOODGOLD

I.R.I.G.M. - B.P. 68
38402 ST. MARTIN D'HERES
CEDEX, FRANCE
ATTN: DR. M. BOUCHON

MINISTRY OF DEFENSE
PROCUREMENT EXECUTIVE
BLACKNESS, BRIMPTON
READING RG7-4RS ENGLAND
ATTN: DR. D. BOWERS

DISTRIBUTION LIST
DTRA-TR-01-15

NTNF/NORSAR
P.O. BOX 51
N-2007 JKELLER, NORWAY
ATTN: DR. F. RINGDAL
ATTN: T. KVAERNA
ATTN: S.MYKKELTVEIT

OBSERVATORIE DE GRENOBLE
I.R.I.G.M. - B.P. 53
38041 GRENOBLE, FRANCE
ATTN: DR. M. CAMPILLO

OBSERVATORIO SAN CALIXTO
INDABURO #944
CASILLA 12656
LA PAZ, BOLIVIA
ATTN: E. MINAYA

RESEARCH SCHOOL OF EARTH SCIENCES
INSTITUTE OF ADVANCED STUDIES
G.P.O. BOX 4
CAMBERRA 2601, AUSTRALIA
ATTN: PROF B.L. N. KENNETT

PTS/CTBTO
VIENNA INTERNATIONAL CENTRE
P.O. BOX 1200
VIENNA A-1400, AUSTRIA
ATTN: P. BASHAM
ATTN: DR. P. FIRBAS
ATTN: DR. R. KEBEASY

RUHR UNIVERSITY/BOCHUM
INSTITUTE FOR GEOPHSIK
P.O. BOX 102148
463 BOCHUM 1, GERMANY
ATTN: PROF H.P. HARJES

SOCIETE RADIOMANA
27 RU CLAUDE BERNARD
75005 PARIS, FRANCE
ATTN: DR. B. MASSINON
ATTN: DR. P. MECHLER

UNIVERSITY OF BERGEN
INSTITUTE FOR SOLID EARTH PHYSICS
ALLEGATION 41
N-5007 BERGEN, NORWAY
ATTN: E. HUSEBYE

UNIVERSITY OF CAMBRIDGE
DEPARTMENT OF EARTH SCIENCES
MADINGLEY RISE, MADINGLEY ROAD
CAMBRIDGE CB3 0EZ, ENGLAND
ATTN: PROF K. PRIESTLEY

DEPARTMENT OF DEFENSE CONTRACTORS

BATTELLE MEMORIAL INSTITUTE
MUNITIONS & ORDNANCE CTR
505 KINGS AVENUE
COLUMBUS, OH 43201 2693
ATTN: TACTEC

BBN CORPORATION
1300 N 17TH STREET SUITE 1200
ARLINGTON, VA 22209
ATTN: DR. D. NORRIS
ATTN: R. GIBSON
ATTN: J. PULLI

CENTER FOR MONITORING RESEARCH
1300 N.17TH STREET, SUITE 1450
ARLINGTON, VA 22209 2402
ATTN: DR. K. L. MCLAUGHLIN
ATTN: DR. R. WOODWARD
ATTN: DR. R. NORTH
ATTN: DR. V. RYABOY
ATTN: DR. X. YANG
ATTN: LIBRARIAN
ATTN: DR. T. J. BENNETT
ATTN: J. MURPHY
ATTN: I. BONDAR
ATTN: DR. B. KOHL

ENSCO, INC
P.O. BOX 1346
SPRINGFIELD, VA 22151 0346
ATTN: D. BAUMGARDT
ATTN: Z. DER

DISTRIBUTION LIST
DTRA-TR-01-15

ITT INDUSTRIES
ITT SYSTEMS CORPORATION
1680 TEXAS STREET SE
KIRTLAND AFB, NM 87117 5669
2 CYS ATTN: DTRIAC

JAYCOR
1410 SPRING HILL ROAD, SUITE 300
MCELAN, VA 22102
ATTN: DR. C.P. KNOWLES

MISSION RESEARCH CORPORATION
8560 CINDERBED ROAD, SUITE 700
NEWINGTON, VA 22122
ATTN: DR. M. FISK
ATTN: R. BURLACU

MULTIMAX, INC
1441 MCCORMICK DRIVE
LANDOVER, MD 20785
ATTN: DR. I.N. GUPTA
ATTN: DR. W. CHAN
ATTN: W. RIVERS

MULTIMAX INC
1090 N HIGHWAY A1A SUITE D
INDIALANTIC, FL 32903
ATTN: DR. H. GHALIB

SCIENCE APPLICATIONS INT'L CORPORATION
10260 CAMPUS POINT DRIVE
SAN DIEGO, CA 92121 1578
ATTN: DR. G. E. BAKER
ATTN: DR. J. STEVENS
ATTN: DR. D. ADAMS
ATTN: DR. M. ENEVA

SCIENCE APPLICATIONS INTERNATIONAL CORP
1227 S. PATRICK DR SUITE 110
SATELLITE BEACH, FL 32937
ATTN: DR. M. FLEIX
ATTN: DR. H. GIVEN

URS CORPORATION
566 EL DORADO STREET
PASADENA, CA 91109 3245
ATTN: DR. B.B. WOODS
ATTN: DR. C. K. SAIKIA
ATTN: DR. G. ICHINOSE

WESTON GEOPHYSICAL CORPORATION
411 NW 26TH ST
GAINESVILLE, FL 32607
ATTN: DR. S. RUSSELL

WESTON GEOPHYSICAL CORPORATION
57 BEDFORD ST, SUITE 102
LEXINGTON, MA 02420
ATTN: DR. D. REITER
ATTN: J. LEWKOWICZ
ATTN: DR. A. ROSCA
ATTN: DR. I. TIBULEAC
ATTN: M. JOHNSON

WESTON GEOPHYSICAL CORPORATION
917 ELLIS AVE SUITE 222
LUFKIN, TX 75904
ATTN: DR. J. BONNER